Control Design to Reduce the Effects of Torsional Resonance in Coupled Systems

A Thesis

Submitted to the Faculty

of

Drexel University

by

Daniel M. Lofaro

in partial fulfillment of the

requirements for the degree

of

Master of Science in Electrical Engineering

June 2008

Dedication

To Mommy and Daddy

Table of Contents

List of Figures

List of Equations

List of Tables

List of Appendices

Symbol Definitions

TR: Torsional Resonance

w_r: Resonance Frequency (rad/sec)

w_{ar}: Anti-Resonance Frequency (rad/sec)

RE: Resonance Equalization

SMC: Sliding Mode Control

SVF: State Variable Feedback

s: Laplace Variable

J_a: Actuator/Motor Inertia (oz-in-sec^2)

J_L: Load Inertia (oz-in-sec^2)

B_a: Actuator/Motor Damping (oz-in/kRPM)

B_L: Load Damping (oz-in/kRPM)

B_c: Coupler Damping (oz-in/kRPM)

K_c: Coupler Spring Constant (oz/in)

T_{in} : Torque Input (ft-lb)

θ_a: Actuator/Motor Angular Position (rad)

θ_L: Load Angular Position (rad)

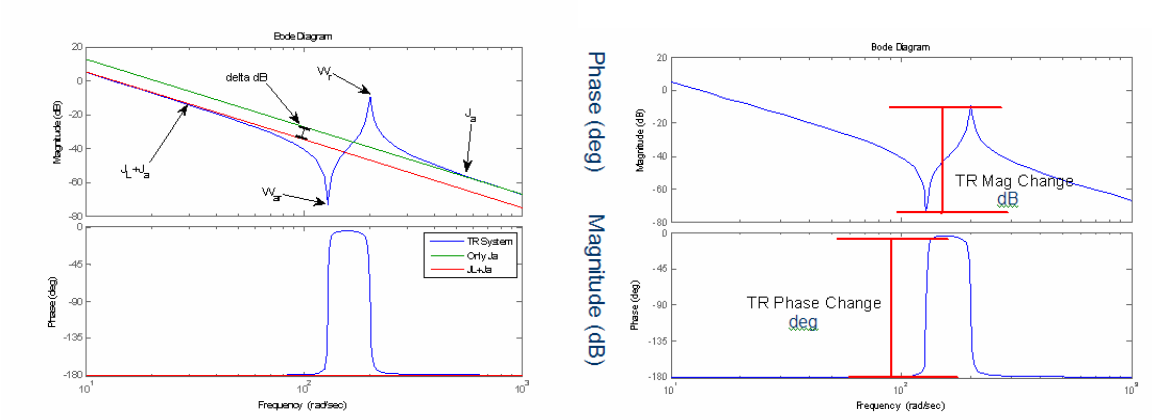

Abstract
Control Design to Reduce the Effects of Torsional Resonance in Coupled Systems
Daniel M. Lofaro
Advisors: Dr. Tom Chmielewski, Dr. Paul Kalata

Connecting two rotary mechanical devices utilizes a flexible coupler to accommodate various shaft misalignments. These couplers, including belts and gear boxes, exhibit a spring constant and a viscous damping term. The spring constant causes the system to have a resonant frequency while the damping controls its amplitude. In the frequency domain this characteristic is called Torsional Resonance (TR). The TR frequencies can not be allowed into the pass band of closed loop servo because it will cause instability.

Some conventional solutions to obtain stable operation include: reduction of the servo's bandwidth below the TR frequencies; using stiffer, more expensive, components to increase the TR frequencies thus increasing the useable bandwidth; and using notch filters to reduce the resonant peak.

The objective of this work is provide a control solution to allow systems using elastic parts, including loose belt drives and plastic gears, achieve sufficient bandwidth to obtain their desired performance. A model of a commercial application exhibiting the TR characteristic has been made using Matlab and Simulink.

A test rig has been constructed with a brushless DC motor and a system able to control the location of the TR frequencies. This test rig is controlled by a hard real time target control system which accepts control through Matlab and Simulink.

The techniques described by Bigley and Rizzo and non-linear Sliding Mode Control (SMC), which has shown to reduce the error at resonance by approximately 50dB, is desired to be modeled and implemented on the physical system. The ability to reduce the effects of TR using electrical control allows mechanical system implementation using less costly components while achieving the desired specifications.

I. Objective

a. *Problem Statement*

When connecting two rotary mechanical devices a coupler is used to connect them. These include the use of 1:1 flexible shaft couplers, to compensate for possible shaft misalignments, as well as belts, and gear boxes. In theory it is desired to have the given coupler be perfectly rigid, ever degree the actuator turns the connected load will turn to its exact location denoted by the input and the gear ratio. For a coupler to be perfectly rigid the latter must be true for all time. In reality gear boxes and couplers are not perfectly rigid and have spring and damping terms associated with them. The spring constant causes the system to have two resonant frequencies collectively called the Torsional Resonance (TR). The TR frequencies, which are referred to as the resonant frequency, w_r, and the anti-resonant frequency, w_{ar}, can not fall within the pass-band of the closed loop servo because it will cause instability.

Figure 1 shows a diagram of an ideal coupled system (Left) and a system exhibiting TR (Right). The ideal system can be reduced to a single acting inertia of J_a+J_L while the system exhibiting TR is connected by a spring damper system thus that reduction can not be made.

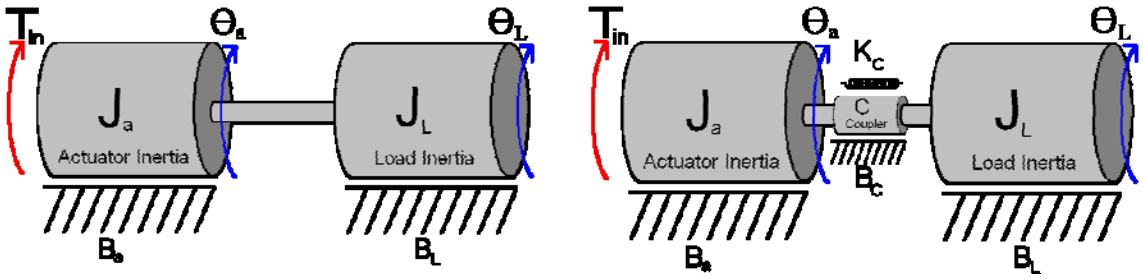

Figure 1: Ideal Coupled System Without TR (Left), System Exhibiting TR (Right)

The ideal frequency response of the ideal coupled system, with θ_a as the output and T_{in} as the input, can be found in Figure 2 on the left graph. The magnitude portion of the frequency response is a straight line with a slope of negative 40dB/dec. The phase of the latter system does not change. The frequency response of the system exhibiting TR can be found in Figure 2 on the right plot. It can be noted that at resonance there

is a peak. This peak reduces the gain margin of the system. The phase also changes around the resonance which reduces the phase margin.

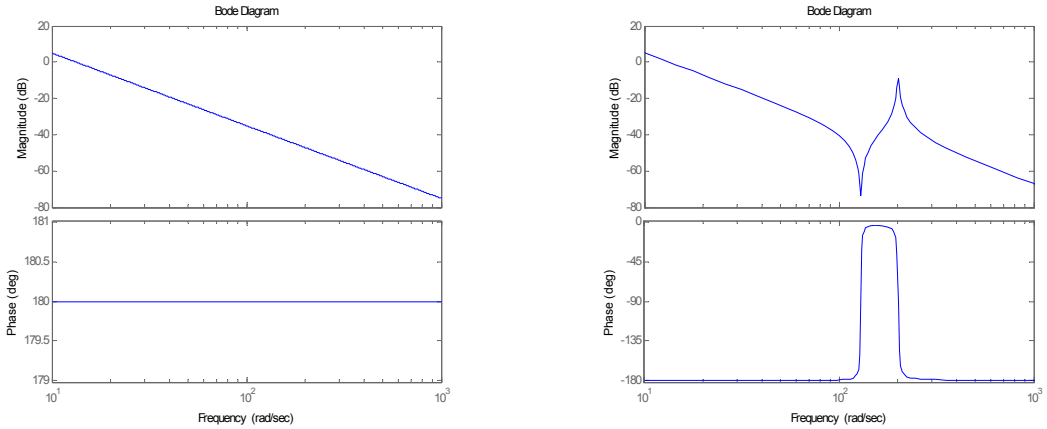

Figure 2: Frequency Response of Desired Coupled System (Left), Frequency Response of System Exhibiting TR (Right)

Contemporary ways of reducing this problem include:

- Reducing the servo's bandwidth so it does not include the TR frequencies. (Appendix E)
- Increasing the couplers spring constant K_c via using higher quality and anti backlash mechanical couplers and gearboxes to push the TR frequencies higher. (Appendix G)
- Using notch filters to reduce the resonant peak. (Appendix D)

Reducing the bandwidth of the servo means that the designed system will not be able to respond as quickly to an input stimulus. Using higher quality and anti-backlash mechanical couplers and gearboxes will give you greater bandwidth but will also include a higher materials price tag. It is also important to note that the use of notch filters is only useful in systems where the TR does not change. Most systems that have TR present tend to have nonlinear, and time varying, elements, including dynamic loads, that will cause the TR frequency to change thus making the notch filter less effective in the ideal case.

b. *Designs to be Considered in this Work*

i. Resonance Equalization (RE) as introduced by W.J. Bigley and V. Rizzo

W. J. Bigley and V. Rizzo presented a technique for, as they describe it, "eliminating the destabilizing effect of mechanical resonance in feedback control systems." [1] The goal of their research was to make a wide band high performance closed loop servo system. In their research Bigley and Rizzo found a relationship between the torque, or current, on the DC motor and the velocity of the shaft. They found that when the current is at its maximum the velocity is at a minimum, no matter where the resonance or anti resonance occurs, see Figure 27. Thus feeding back the velocity and torque states would compensate for the effects of TR no matter where it occurs even when the parameters of the system changes.

ii. Sliding mode control (SMC)

Sliding mode control (SMC) is also a good candidate for a method to reduce the effects of TR. This is because SMC is a robust control method that is able to properly control a system even when parameters are not precisely known. The main idea about SMC is that you are able to make a control that will guarantee the performance of a system in u and x, see Figure 31, within a given error φ and ε respectively. When using SMC one, or more, parameters are chosen to be unknown. The *unknown* parameters are given a range that they are able to be between and still have the system perform properly.

II. Background

c. *Model*

A system with TR typically consists of three main items:

- An actuator, or motor, with a given inertia, J_a, and damping, B_a, associated with it.
- An inertial load, J_L, with a given damping, B_L, associated with it.
- A coupler between the actuator and the load with a spring constant, K_C, and a damping, B_C, associated with it.

It is assumed that the inertia of the coupler is included in the inertia of the actuator and the load, see Figure 4. The physical diagram of the system with TR can be found in Figure 3. In order to find the transfer function for this system, where T_{in} is the torque input and the actuator angle θ_a is the output, the physical diagram is then converted into a mechanical network, see Figure 4, so the system's dynamic equations can be written.

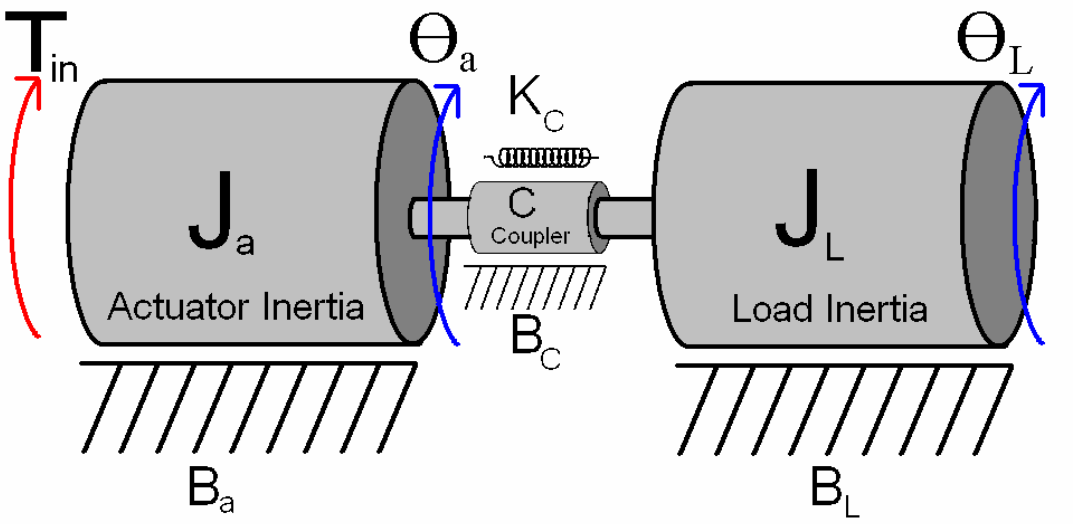

Figure 3: Physical Diagram of the system exhibiting TR

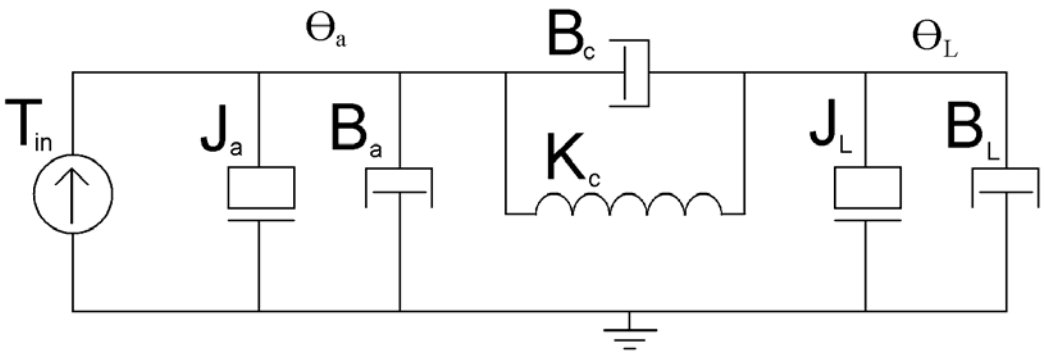

Figure 4: Mechanical Schematic Drawling of System with TR

d. *Transfer Function $\theta_a/T(s)$ Calculation*

See Equation 1 and Equation 2 for the time equations for the system from Figure 4.

$$T(t) = J_a \ddot{\theta}_a + (B_a + B_c)\dot{\theta}_a + K_c \theta_a - (K_c \theta_L + B_c \dot{\theta}_L)$$

Equation 1: Time Equation for TR System from Figure 4 at θ_a Node

$$0 = J_L \ddot{\theta}_L + (B_L + B_c)\dot{\theta}_L + K_c \theta_L - (K_c \theta_a + B_c \dot{\theta}_a)$$

Equation 2: Time Equation for TR System from Figure 4 at θ_L Node

Convert time equations to the Laplace domain.

$$T(s) = (s^2 J_a + sB_a + K_c + sB_c)\theta_a - (K_c + sB_c)\theta_L$$

Equation 3: Laplace Transformation of Equation 1

$$0 = (s^2 J_L + sB_L + K_c + sB_c)\theta_L - (K_c + sB_c)\theta_a$$

Equation 4: Laplace Transformation of Equation 2

Solve for $\theta_a(s)/T(s)$

$$\theta_L(s) = \frac{(K_c + sB_c)}{(s^2 J_L + sB_L + K_c + sB_c)}\theta_a$$

Equation 5: Solve for θ_L from Equation 4

$$\frac{\theta_L}{\theta_a} = \frac{(K_c + sB_c)}{(s^2 J_L + sB_L + K_c + sB_c)}$$

Equation 6: Relationship between θ_L and θ_a

Equation 6 shows the relationship between θ_L and θ_a as the ratio of θ_L / θ_a. Note that θ_a contains up to and including first order terms and θ_L includes up to and including second order terms.

$$T(s) = (s^2 J_a + sB_a + K_c + sB_c)\theta_a - \frac{(K_c + sB_c)(K_c + sB_c)}{(s^2 J_L + sB_L + K_c + sB_c)}\theta_a$$

Equation 7: Replace θ_L from Equation 3 with θ_L in Equation 5

$$\frac{\theta_a(s)}{T(s)} = \frac{s^2 J_L + sB_L + K_c + sB_c}{(s^2 J_a + sB_a + K_c + sB_c)(s^2 J_L + sB_L + K_c + sB_c) - (K_c + sB_c)^2}$$

Equation 8: Solve for $\theta_1(s)/T(s)$ from Equation 7

$$\frac{\theta_a(s)}{T(s)} = \frac{s^2 J_L + sB_L + K_c + sB_c}{s^4 J_a J_L + \left(J_a B_L + B_a J_L + B_c J_a + B_c J_L\right)s^3 + \left(K_c J_a + B_a B_L + B_c B_a + K_c J_L + B_c B_L\right)s^2 + (K_c B_a + K_c B_L)s}$$

Equation 9: Expansion of Equation 8

$$\frac{\theta_a(s)}{T(s)} = \frac{\frac{1}{J_a J_L}\left(s^2 J_L + sB_L + K_c + sB_c\right)}{s^4 + \left(J_a B_L + B_a J_L + B_c J_a + B_c J_L\right)\frac{s^3}{J_a J_L} + \left(K_c J_a + B_a B_L + B_c B_a + K_c J_L + B_c B_L\right)\frac{s^2}{J_a J_L} + (K_c B_a + K_c B_L)\frac{s}{J_a J_L}}$$

Equation 10: Reduction of Equation 9 to a Monic Polynomial

The system described in Equation 1 and Equation 2 can also be described in state space format. See Equation 11 for the latter system shown in state space format.

$$\begin{bmatrix} \ddot{\theta}_a \\ \dot{\theta}_a \\ \ddot{\theta}_L \\ \dot{\theta}_L \end{bmatrix} = \begin{bmatrix} \frac{-(B_a+B_c)}{J_a} & \frac{-K_c}{J_a} & \frac{B_c}{J_a} & \frac{K_c}{J_a} \\ 1 & 0 & 0 & 0 \\ \frac{B_c}{J_L} & \frac{K_c}{J_L} & \frac{-(B_c+B_L)}{J_L} & \frac{-K_c}{J_L} \\ 0 & 0 & 1 & 0 \end{bmatrix} \begin{bmatrix} \dot{\theta}_a \\ \theta_a \\ \dot{\theta}_L \\ \theta_L \end{bmatrix} + \begin{bmatrix} \frac{1}{J_a} \\ 0 \\ 0 \\ 0 \end{bmatrix} T(t)$$

Equation 11: State Space Representation of Single Coupler System with TR from Figure 3

The transfer function $\theta_a(s)/T(s)$ in Equation 10 is the transfer function from the angular position of the actuator, θ_a, with torque, T, as the input term. In this system the damping of the actuator and the load is very small and will be assumed to be zero. Thus the B_a and B_L terms are equal to zero.

$$\frac{\theta_a(s)}{T(s)} = \frac{\frac{1}{J_a J_L}\left(s^2 J_L + K_c + sB_c\right)}{s^4 + \left(B_c J_a + B_c J_L\right)\frac{s^3}{J_a J_L} + \left(K_c J_a + K_c J_L\right)\frac{s^2}{J_a J_L}}$$

Equation 12: Reduction of Equation 10 with B_L and B_a Equal to Zero

$$\begin{bmatrix} \ddot{\theta}_a \\ \dot{\theta}_a \\ \ddot{\theta}_L \\ \dot{\theta}_L \end{bmatrix} = \begin{bmatrix} \frac{-B_c}{J_a} & \frac{-K_c}{J_a} & \frac{B_c}{J_a} & \frac{K_c}{J_a} \\ 1 & 0 & 0 & 0 \\ \frac{B_c}{J_L} & \frac{K_c}{J_L} & \frac{-B_c}{J_L} & \frac{-K_c}{J_L} \\ 0 & 0 & 1 & 0 \end{bmatrix} \begin{bmatrix} \dot{\theta}_a \\ \theta_a \\ \dot{\theta}_L \\ \theta_L \end{bmatrix} + \begin{bmatrix} \frac{1}{J_a} \\ 0 \\ 0 \\ 0 \end{bmatrix} T(t)$$

Equation 13: Reduction of Equation 11 with B_L and B_a Equal to Zero

$$\begin{bmatrix} \ddot{\theta}_a \\ \dot{\theta}_a \\ \ddot{\theta}_L \\ \dot{\theta}_L \end{bmatrix} = \begin{bmatrix} -2.1739 & -23913 & 2.1739 & 23913 \\ 1 & 0 & 0 & 0 \\ 1.5152 & 16667 & -1.5152 & -16667 \\ 0 & 0 & 1 & 0 \end{bmatrix} \begin{bmatrix} \dot{\theta}_a \\ \theta_a \\ \dot{\theta}_L \\ \theta_L \end{bmatrix} + \begin{bmatrix} 434.7826 \\ 0 \\ 0 \\ 0 \end{bmatrix} T(t)$$

Equation 14: State Spaces Representation from Equation 13 with values from Table 1

$$\frac{\theta_a(s)}{T(s)} = \frac{\frac{1}{J_a J_L}\left(s^2 J_L + K_c + sB_c\right)}{s^2\left(s^2 + \frac{B_c\left(J_a + J_L\right)}{J_a J_L}s + \frac{K_c\left(J_a + J_L\right)}{J_a J_L}\right)}$$

Equation 15: Reduction of Characteristic Equation of Equation 12 to show double pole at origin

The transfer function in Equation 15 will be the transfer function that the majority of this paper will be dealing with. Please note that Equation 15 is the transfer function from $\theta_a(s)/T(s)$ where θ_a is the measured angle from the actuator before the coupler. θ_L is the angle measurement after the coupler on the load side.

From the reduction of Equation 12 you can easily see in Equation 15 that there is a double pole at the origin and that there are two complex conjugate poles in the left half plane (LHP). The location of the complex conjugate poles are denoted by the quadratic equation in Equation 16.

$$s = -\frac{B_c\left(J_a + J_L\right)}{2J_a J_L} \pm \frac{1}{2}\sqrt{\left(\frac{B_c\left(J_a + J_L\right)}{J_a J_L}\right)^2 - 4\frac{K_c\left(J_a + J_L\right)}{J_a J_L}}$$

Equation 16: Poles of TR System from Equation 15

$$4K_c > B_c{}^2\left(\frac{J_c + J_L}{J_a J_L}\right)$$

Equation 17: Restrictions on B_c, K_c, J_a and J_L in reference to Equation 16

The value under the radical in Equation 16 is guaranteed to be negative as long as the inequality in Equation 17 holds true. Thus the non-squared term under the radical in Equation 16 will dominate over the squared term. From the latter assumptions we can assume that the complex conjugate poles can be reduced to that of those found in Equation 18.

$$s = -\frac{\left(B_c J_a + B_c J_L\right)}{2 J_a J_L} \pm i \frac{1}{2} \sqrt{4 \frac{\left(K_c J_a + K_c J_L\right)}{J_a J_L} - \left(\frac{\left(B_c J_a + B_c J_L\right)}{J_a J_L}\right)^2}$$

Equation 18: Complex Conjugate Poles with the given assumptions

The over all expectation, in regards to pole placement, for a system with TR is to have two complex conjugate poles and a double pole at the origin. It is important to note that the system as described in Figure 3 is fully controllable. Equation 19 shows that the system is fully controllable by using the state space representation from Equation 13 and showing that the rank of the resulting controllability matrix, Co, has full rank. Equation 20 shows the controllability matrix from Equation 19 with the values from Table 1.

$$A = \begin{bmatrix} \frac{-B_c}{J_a} & \frac{-K_c}{J_a} & \frac{B_c}{J_a} & \frac{K_c}{J_a} \\ 1 & 0 & 0 & 0 \\ \frac{B_c}{J_L} & \frac{K_c}{J_L} & \frac{-B_c}{J_L} & \frac{-K_c}{J_L} \\ 0 & 0 & 1 & 0 \end{bmatrix} \qquad B = \begin{bmatrix} \frac{1}{J_a} \\ 0 \\ 0 \\ 0 \end{bmatrix} \qquad Co = \begin{bmatrix} B & AB & A^2B & A^3B \end{bmatrix}$$

$$Rank(Co) = 4$$

Equation 19: Controllability Matrix based on Equation 13 assuming B_c, J_a, J_L, and K_c less than zero [2]

$$Co = \begin{bmatrix} 434.78 & -945.18 & -1.04E7 & 7.67E7 \\ 0 & 434.78 & -945.18 & -1.04E7 \\ 0 & 658.76 & 7.24E6 & -5.35E7 \\ 0 & 0 & 658.76 & 7.24E6 \end{bmatrix}$$

Equation 20: Controllability matrix based on Equation 19 and the values from Table 1

It has also been found that the system, with the angular position θ_a being the only output, is fully observable. Equation 21 shows that the observability matrix of the system with the latter output has full rank, thus it is fully observable. Equation 22 is the observability matrix from Equation 21 with values given in Table 1.

$$A=\begin{bmatrix} \frac{-B_c}{J_a} & \frac{-K_c}{J_a} & \frac{B_c}{J_a} & \frac{K_c}{J_a} \\ 1 & 0 & 0 & 0 \\ \frac{B_c}{J_L} & \frac{K_c}{J_L} & \frac{-B_c}{J_L} & \frac{-K_c}{J_L} \\ 0 & 0 & 1 & 0 \end{bmatrix} \qquad C=\begin{bmatrix} 0 & 1 & 0 & 0 \end{bmatrix} \qquad Ob=\begin{bmatrix} C \\ CA \\ CA^2 \\ CA^3 \end{bmatrix}$$

$$Rank(Ob)=4$$

Equation 21: Observability Matrix based on Equation 13 assuming B_c, J_a, J_L, and K_c greater than zero [2]

$$Ob=\begin{bmatrix} 0 & 1 & 0 & 0 \\ 1 & 0 & 0 & 0 \\ -2.17 & -2.39E4 & 2.17 & 2.39E4 \\ -2.39E4 & 8.82E4 & 2.38E4 & -8.82E4 \end{bmatrix}$$

Equation 22: Observability Matrix from Equation 21 with values from Table 1

For the remainder of the paper the values for B_c, B_L, B_a, K_c, J_a, and J_L can be found in Table 1. Equation 23 is the transfer function of the system with TR as seen in Equation 15 with the values given in Table 1. Equation 14 is the state space representation of the TR system as stated in Equation 13 with the values given in Table 1.

In addition please note that the system is:

- Fully Observable:
  - Angular Position of Actuator as the Output
  - Angular Position of Load as the Output

- Not Fully Observable:
  - Angular Velocity of Actuator as the Output
  - Angular Velocity of Load as the Output

Table 1: Values for Figure 3

Inertia 'J' (oz-in-sec^2)	Damping 'B' $\left(\frac{\text{oz-in}}{\text{krpm}}\right)$	Spring 'K' $\left(\frac{\text{oz}}{\text{in}}\right)$
$J_a = 0.0023$	$B_a = 0$	$K_a = 0$
$J_L = 0.0033$	$B_L = 0$	$K_L = 0$
$J_c = 0$	$B_c = 0.005$	$K_c = 55$

$$\frac{\theta_a(s)}{T(s)} = \frac{434.8s^2 + 658.8s + 7.246E^6}{s^2\left(s^2 + 3.689s + 4.058E^4\right)}$$

Equation 23: Transfer Function from Equation 15 with values from Table 1

Figure 5 shows the pole zero plot of the transfer function from Equation 23. Please note that the system has a double pole at the origin.

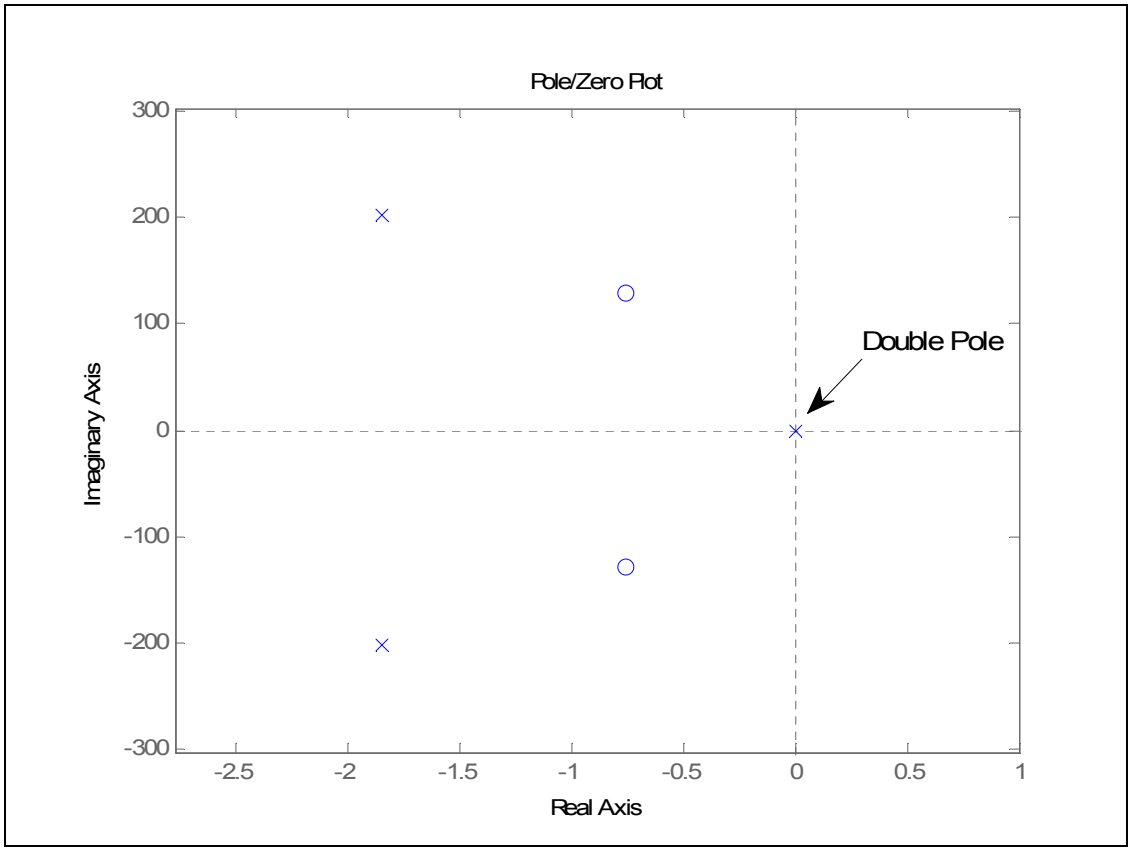

Figure 5: Pole-Zero plot of Equation 23

e. *Frequency Response of Mode*

The TR system from Equation 23 has been shown to have a double pole at the origin and a set of complex conjugate poles in the LHP. The expected effect of this is to have a frequency response, or bode, plot that has a slope of -40dB/dec where the frequency is measured in rad/sec and is plotted on the horizontal axis on a log scale and the y axis is measured in decibels (dB) on a linear scale. The presents of the two complex conjugate poles denote an expected disturbance at the resonant frequencies. When the frequency response of the system from Equation 23, with the parameters from Table 1 is plotted we see that there is a dip and a spike in the plot at approximately 129rad/sec and 201rad/sec respectively. Figure 6 shows the frequency response plot of the system with TR. The latter plot was found by the use of the bode() function in Matlab on Equation 23. The frequencies at which the dip and peak occur are denoted by the use of the data label built in to the graph function in Matlab.

The dip in Figure 6 is called the anti-resonance, w_{ar}, which is due to the complex conjugate zeros. The peak is called the resonance, w_r, which is due to the complex conjugate poles. The locations of the w_{ar} and w_r can be calculated by Equation 24 [1].

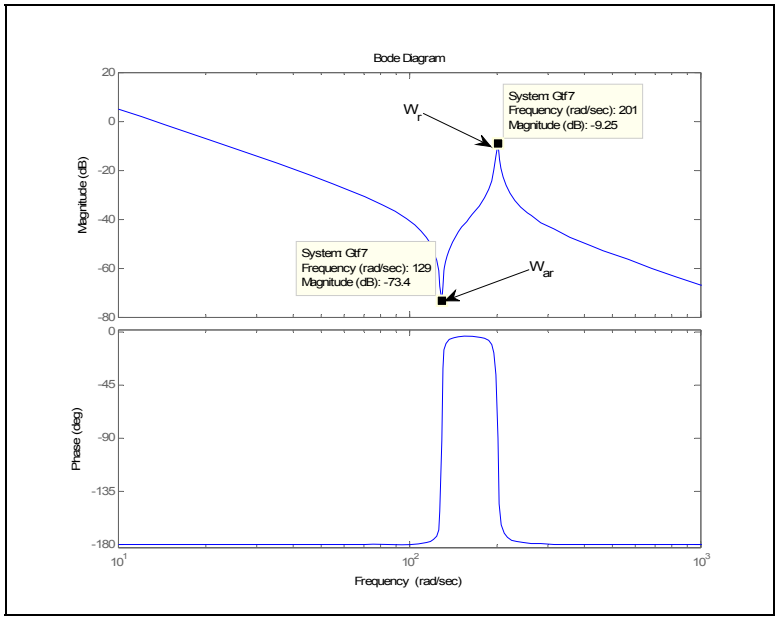

Figure 6: Frequency Response of TR System from Equation 23 with parameters from Table 1

$$w_{ar} = \left(\frac{K_c}{J_L} \right)^{\frac{1}{2}} \qquad w_r = \left(\frac{K_c}{\left(\frac{J_a J_L}{J_a + J_L} \right)} \right)^{\frac{1}{2}}$$

Equation 24: Calculation of w_{ar} and w_r frequencies in rad/sec [1]

By the use of Equation 24 and the parameters from Table 1 the w_r and w_{ar} frequencies that were previously state are validated. The calculated value of w_{ar}, via the use of Equation 24, is found in Equation 25. This value is equal to that of the w_{ar} found in the frequency response plot in Figure 6. The calculated value of w_r, via the use of Equation 24, is found in Equation 26. This value is equal to that of the w_r found in the frequency response plot in Figure 6.

$$w_{ar} = \left(\frac{K_c}{J_L} \right)^{\frac{1}{2}} = \left(\frac{55}{0.0033} \right)^{\frac{1}{2}} = 129.1 \frac{rad}{\text{sec}}$$

Equation 25: Calculation of w_{ar} using parameters from Table 1 and Equation 24

$$w_r = \left(\frac{K_c}{\left(\frac{J_a J_L}{J_a + J_L} \right)} \right)^{\frac{1}{2}} = \left(\frac{55}{\left(\frac{0.0023 \square 0.0033}{0.0023 + 0.0033} \right)} \right)^{\frac{1}{2}} = 201.4 \frac{rad}{\text{sec}}$$

Equation 26: Calculation of w_r using parameters from Table 1 and Equation 24

Note that the useable bandwidth of the system with TR is limited to frequencies below w_r. Knowing the w_{ar} and w_r frequencies means that the upper limit for the bandwidth is known.

The effect on the frequency response of the transfer function $\theta_a(s)/T(s)$ on the TR system from Figure 3 with the addition of damping on the load and actuator can be found in Appendix B.

In addition, to show that TR exists in physical systems a test rig was created and the TR was measured using the Real Time system described in Appendix F. See Figure 7 for the frequency response of a physical, real life, system containing TR.

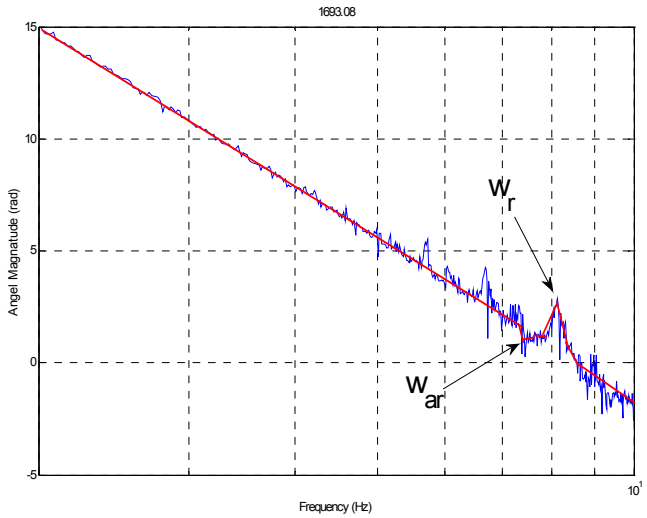

Figure 7: Frequency response plot of physical system with TR from Appendix F

Note the dip and peak at the w_{ar} and w_r frequencies respectively on Figure 7. This shows that TR does occur in coupled systems.

f. *Effects of TR on Effective Load*

The dipping and peaking of the magnitude of the frequency response plot of a system with TR is not the only effect that TR has on the system. Another effect is a change in the effective load seen by the system before w_{ar} to after w_r, see Figure 8. Before the w_{ar} the acting inertial load on the system is the sum of the actuator's inertial load, J_a, and the load's inertial load, J_L. This is a second order system with a slope of negative 40dB/dec on the frequency response plot. After the w_r the acting inertial load is only the actuator's inertia, J_a, which also defines a second order system with a slope of negative 40dB/dec on the frequency response plot. The latter characteristics can be seen in the frequency response plot in Figure 8. It can be noted that there is an offset between the frequency responses of the second order estimations of the system with TR when going from before the w_{ar} to after the w_r when looking at the magnitude in dB of

the response. This offset, known as gain separation, means that there is a parameter, in this case the effective inertia on the system, which is changing. Figure 8 shows the frequency response of the system with TR from Figure 3 and values from Table 1 with the added frequency responses of a systems with out TR but having the effective load as J_L+J_a and J_a. The equations for the transfer functions of the system with the effective load of J_L+J_a and J_a can be found in Equation 27 and Equation 28 respectively.

Please note that a common method to reduce the change in the effective inertial load is to make the actuator's inertial load much less than that of the load's inertial load.

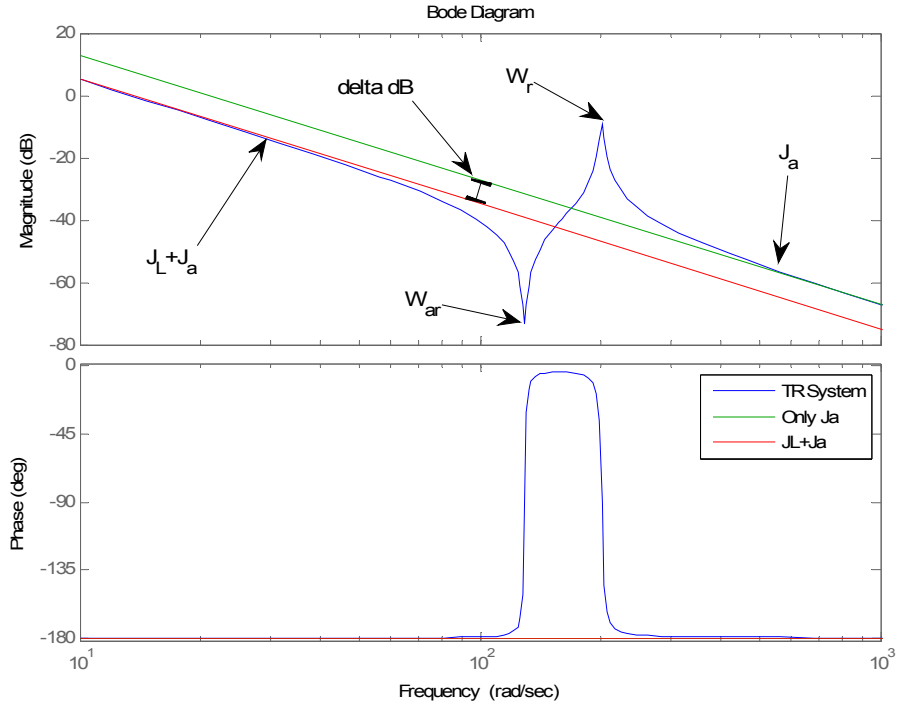

Figure 8: Frequency Response Plot of System with TR from Equation 23, System with no TR with inertial load of J_a, and System with no TR and inertial load of J_a+J_L

$$\frac{\theta_{(J_a+J_L)}(s)}{T(s)} = \frac{1}{(J_a+J_L)s^2}$$

Equation 27: Transfer function for a mass spring damper system with effective load of J_a+J_L, zero damping and zero spring constant

$$\frac{\theta_{J_a}(s)}{T(s)} = \frac{1}{J_a s^2}$$

Equation 28: Transfer function for a mass spring damper system with effective load of J_a, zero damping and zero spring constant

The gain separation when going from an acting load of J_L+J_a to J_a can be calculated via the use of Equation 29.

$$\Delta dB = 40 \log_{10}\left(\frac{\omega_r}{\omega_{ar}}\right)$$

Equation 29: Gain Separation Equation [14]

g. *Stability*

As shown in Equation 30 all of the poles are located in the LFP or located at the origin. Because there is more than a single pole located at the origin the system is not BIBO stable, it is marginally stable [1][3]. It is also important to note that when examining the frequency response of the TR system from Equation 23 and Figure 6 the system is shown to go unstable between w_{ar} and w_r on the frequency axis. One of the major causes of the instability can be seen in the frequency response plot of the system with TR in Figure 6. It can be noted from the plot that the gain margin of the open loop system has been drastically reduced by the TR. In this case the gain margin has been reduced to 9.25dB. The second problem is that the phase of the system flips by about 180^o, or π rad, in the area around w_{ar} and w_r. Due to the latter it is concluded that the system is marginally stable. The system is stable for input frequencies that do not include the w_{ar} or w_r frequencies.

$$s_1 = 0$$
$$s_2 = 0$$
$$s_3 = -1.845 + 210.44$$
$$s_4 = -1.845 - 210.44$$

Equation 30: Poles of the TR System in Equation 23 with parameter from Table 1

The frequency that the system has the potential of oscillating at can be found by looking at the second order part of the characteristic equation in Equation 15, i.e. without the two zeros at the origin, and comparing it with the characteristic equation from Equation 31. It can be noted that the frequency of oscillation is equal to 201.44rad/sec, Equation 32, which matches that of w_r from Equation 26.

$$G(s) = \frac{\omega_n^{\,2}}{s^2 + 2\xi\omega_n s + \omega_n^{\,2}}$$

Equation 31: General Second Order Transfer Function [2] where ξ is the damping coefficient and ω_n is the natural frequency

$$\omega_n = \sqrt{\frac{K_c\left(J_a + J_L\right)}{J_a J_L}} = 201.44\frac{rad}{\sec}$$

Equation 32: Frequency of oscillation for system from Equation 15, parameters from Table 1

When looking at the root locust of the system with TR and the input being torque and the output being θ_a, i.e. the transfer function $\theta_a(s)/T(s)$ as described in Equation 10 it can be noted that when put in a unity gain closed loop configuration the system will go unstable for higher gains. The system goes unstable because for higher gains the two complex conjugate poles, and the double pole at the origin, all move to the right half plane (RHP). Thus at higher gains the system is not BIBO stable.

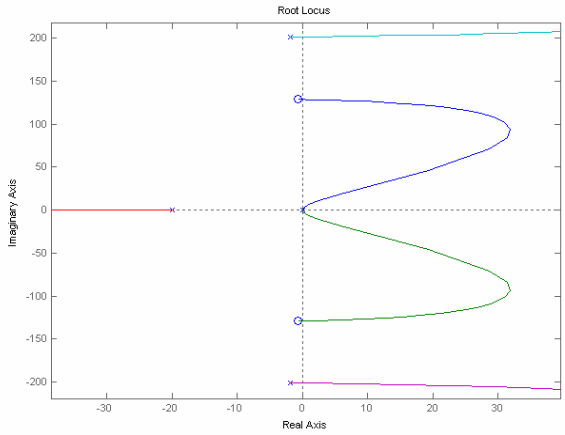

Figure 9: Root Locust of the system with TR with the transfer function $\theta_a(s)/T(s)$ Equation 10 and in a unity gain negative feedback control loop with K_p=50

h. *Matlab Simulink Model of System with TR*

The TR system as shown in Figure 3 and described in Equation 1 and Equation 2 has been put in to Matlab's Simulink for use in the implementation of different control schemes, including SMC and that as described by Rizzo [1]. As stated previously the assumption is that B_a and B_L are equal to zero.

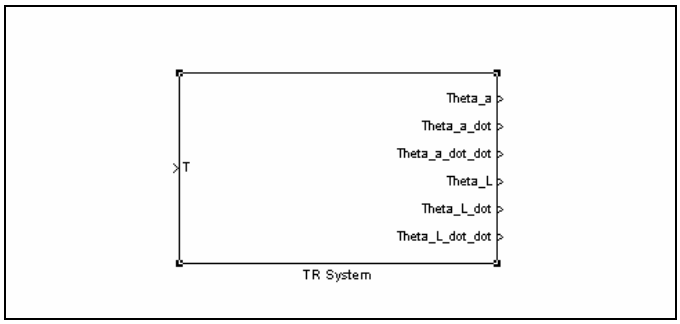

Figure 10: Simulink Model of TR System as Described in Equation 1 and Equation 2

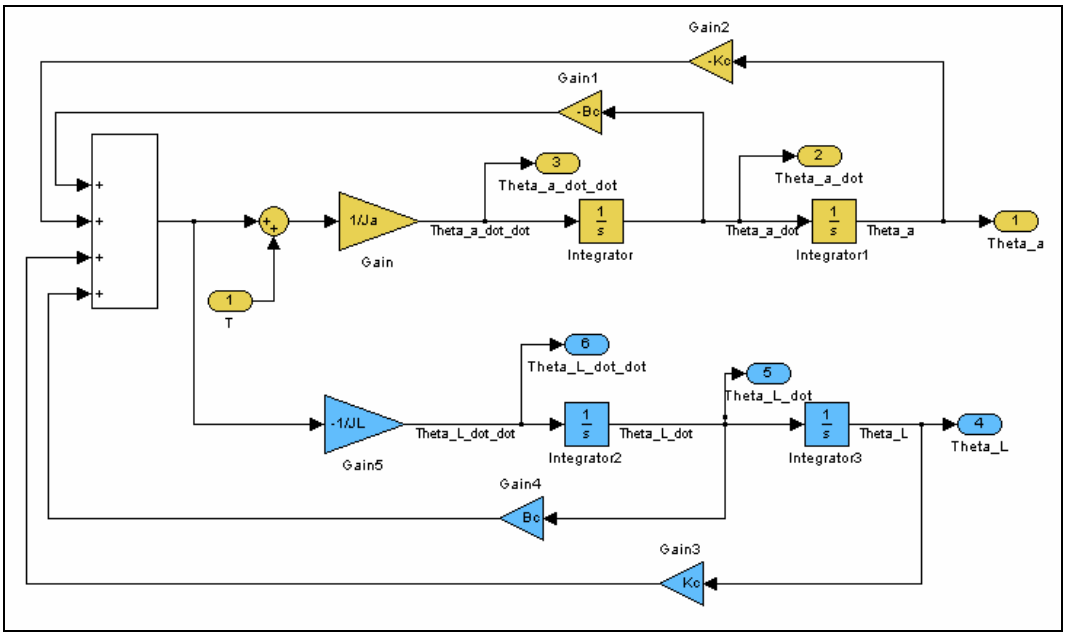

Figure 11: Inside of the Simulink Model of TR System as shown in Figure 10

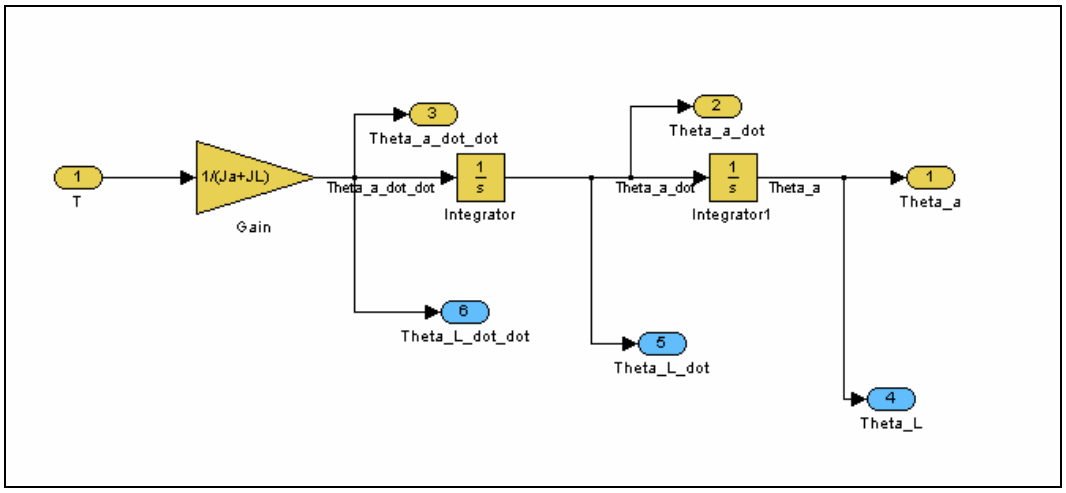

Figure 12: Inside of the "No TR System" block. Contains that Simulink model of the system as if it had a perfectly non-elastic and non-damping coupler. The total inertial load is given as J_L+J_a

Figure 10 and Figure 11 show the Simulink model of TR system from Figure 3. The top colored section of Figure 11 is referencing the actuator and the bottom section is referencing the load. The system has an input of torque, which only acts on the actuator side. Due to the fact that it was shown that the system was fully observable in Equation 21 the output consists of all of the states of the TR system; the angular position, angular velocity, and angular acceleration of both the actuator and the load. For ease of simulation these states will be used directly but can be also be found by the use of a partial or full state observer [2][3].

To ensure that each of the different representations of the TR system form Figure 3 was represented correctly the frequency response of three different forms of the TR systems were plotted on top of each other. The transfer function form (blue), Equation 23, was plotted on the same plot as the state space form (Green), Equation 14, and the Simulink model (Red), Figure 11. The latter plot, Figure 13, shows that each of the magnitudes do fall on top of each other. Though the phases of the different representations do not fall on top of each other it is important to not that they are still considered the same because the system is simply 360^o, or 2π rad, out of phase which reduces to being 0^o, or 0 rad, out of phase. Thus the systems are in phase with each other and thus the systems are verified to be the same. Though the simulation works with different solvers please note that all Simulink simulation are being solved with the Ode5 (Dormand-Price) solver with a sampling period of 0.0001sec.

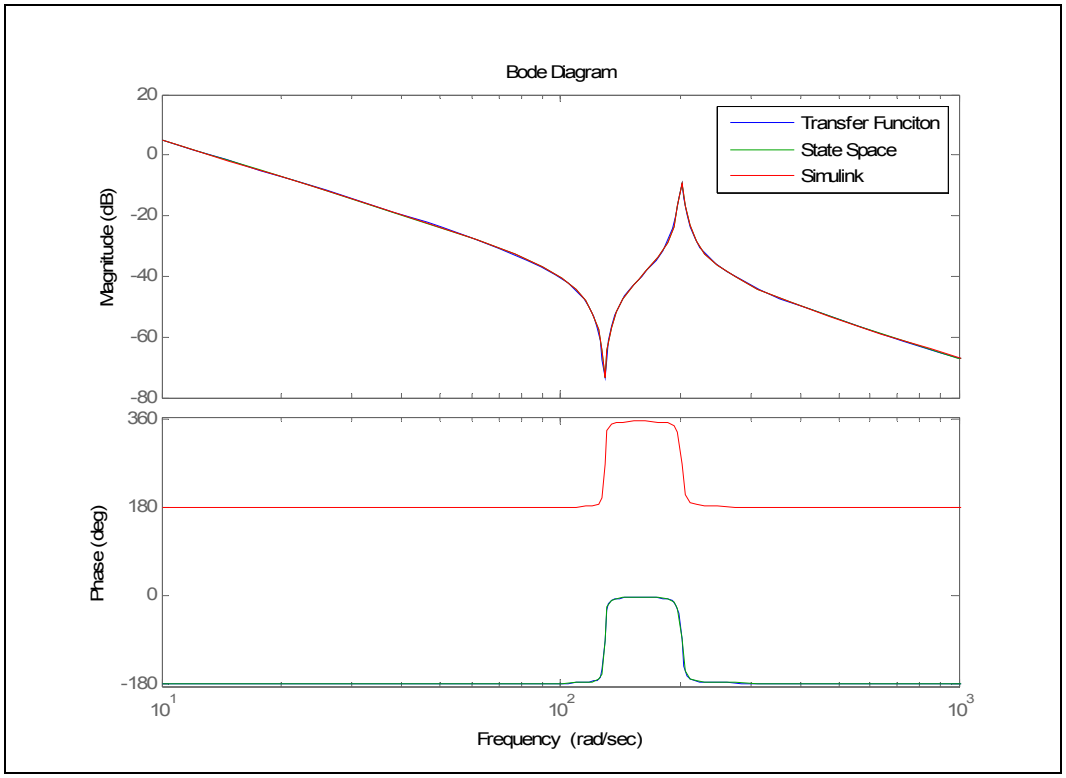

Figure 13: Frequency Response of System from Figure 3 using the Transfer Function, Equation 23, State Space Representation, Equation 14, and Simulink Model, Figure 11, using θ_a as the output state and T as the input.

See Appendix for the calculation of the transfer function $\theta_L(s)/T(s)$ as well as the comparison between the frequency responses of $\theta_a(s)/T(s)$ and $\theta_L(s)/T(s)$.

i. *Effects On Velocity Trajectory*

When there is a step torque command input to the system, like that seen in Figure 14, the output velocity exhibits an oscillatory behavior. The frequency of oscillation is expected to be equal to w_r of the system from Equation 26. Therefore this should have a ripple frequency of 201.4 rad/sec, 32.1 Hz.

Figure 14 shows the torque input to the system with TR. This torque input is acting on the only input of Figure 10. Note that the torque input from Figure 14 is zero mean.

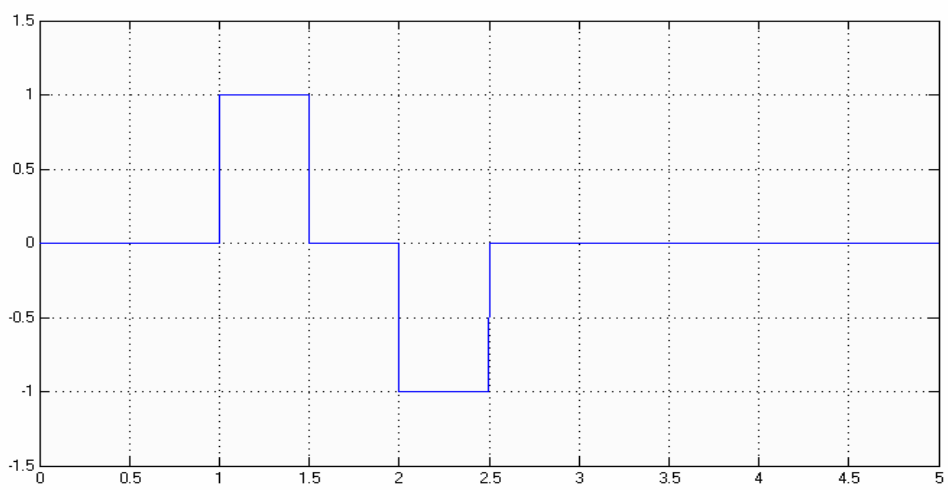

Figure 14: Step Torque Input to TR System from Figure 10. Vertical Axis is Magnitude, Horizontal Axis is Time in sec.

Figure 15 shows the actuator velocity output of the system with TR from Figure 10 as well as the actuator velocity output of the system with out TR from Figure 12. The latter output is the response to the torque input from Figure 14. It is important to note that though the mean of the angular velocity responses to the torque input are the same for both the system with TR and the system with out TR in Figure 15, the system with TR does not follow the ideal system's trajectory, i.e. the system with out TR. The system with TR has a decaying oscillation around the response of the system with out TR.

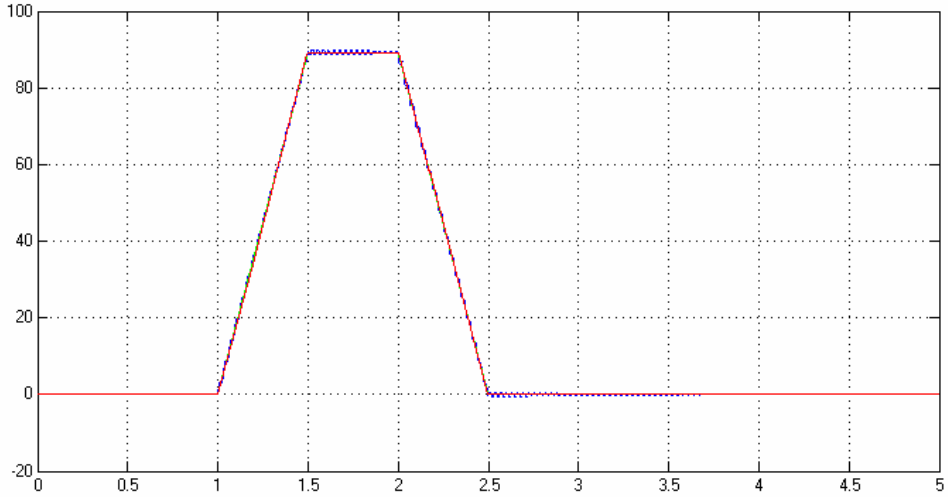

Figure 15: Angular Velocity of the Actuator Shaft of the system with TR (Yellow), Angular Velocity of the Actuator Shaft of the system without TR (Pink) due to Input of Figure 14. Vertical Axis is Magnitude, Horizontal Axis is Time in sec.

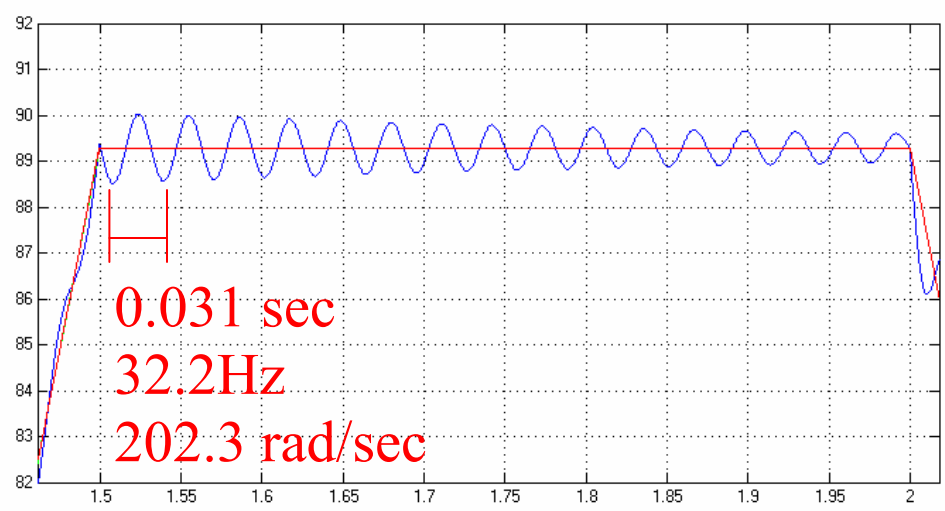

Figure 16: Angular Velocity of the Actuator Shaft of the system with TR (Blue), Angular Velocity of the Actuator Shaft of the system without TR (Red) due to Input of Figure 14 zoomed in from 1.5 to 2.0 sec. Vertical Axis is Magnitude, Horizontal Axis is Time in sec.

Figure 16 shows Figure 15 magnified about 1.5 sec to 2 sec. Note that in Figure 16 the angular velocity of the actuator shaft has a decaying sinusoid on it. The decaying sinusoid operates around the output of the system with a perfect coupler, i.e. a system with out TR. It can be noted that the frequency of the decaying sinusoid seen in Figure 16 on the angular velocity plot of the actuator shaft due to the input from Figure 14 has a period of approximately 0.031sec and a frequency of 32.2 Hz, 202.3 rad/sec. This frequency is the same as the w_r computed in Equation 26, as well as the expected oscillation frequency as calculated in Equation 32. This confirms that the ripple is caused by the coupling device which creates the TR.

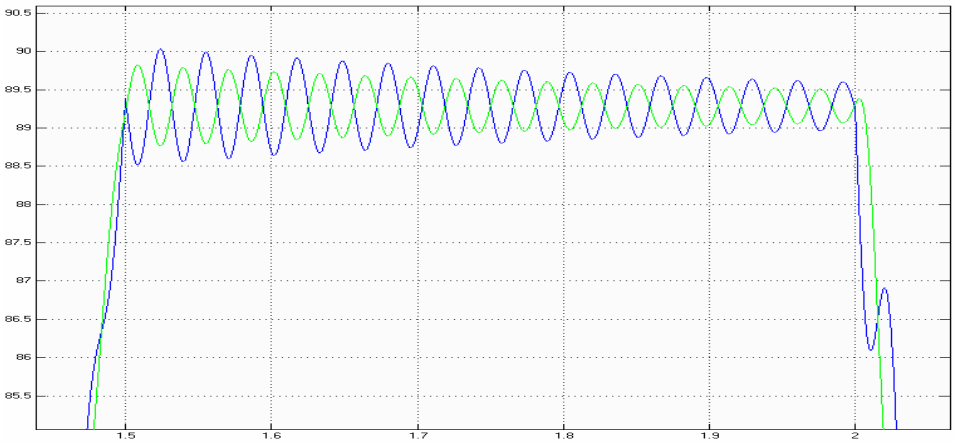

Figure 17: Plot Angular Velocity of the Load (green) and the Actuator (blue) due to the Input of Figure 14. Vertical Axis is Magnitude, Horizontal Axis is Time in sec.

Figure 17 shows that the angular velocity of the load is 180^o out of phase with the angular velocity of the actuator. They also have different magnitudes. These magnitudes are partially dependent on the ratio of the coupler being used. In this experiment the ratio of the input to the output of the coupler is 1:1.

The Simulink diagram used to create the plots due to the input Figure 14 can be found in Figure 18.

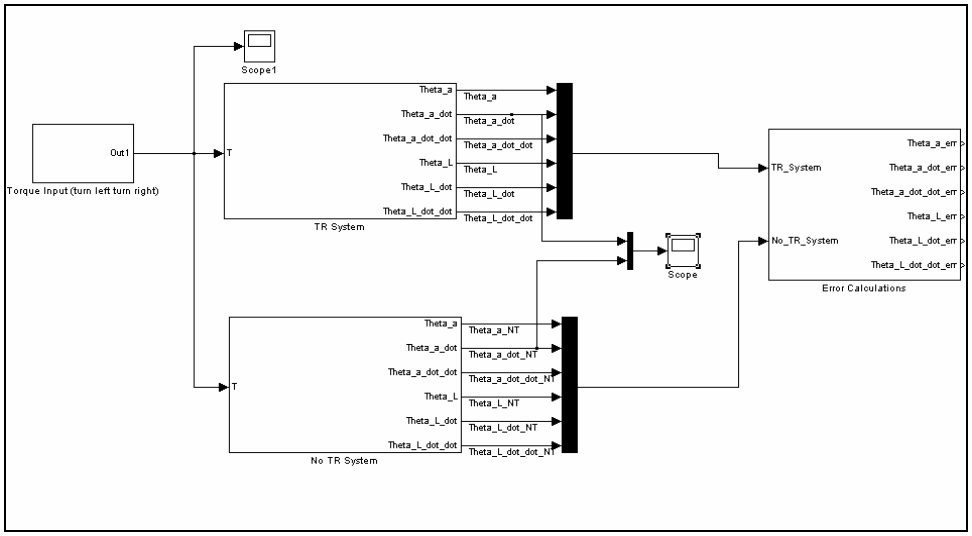

Figure 18: Simulink Diagram for Plotting Angular Velocity on the Actuator shaft and the Load Shaft

The error plots, $\theta_{(\text{With TR})} - \theta_{(\text{Without TR})}$, of the actuator and load position vs. the system without TR is can be found in Figure 19 and Figure 20 respectively.

Note that the observed error, $\theta_{(\text{With TR})} - \theta_{(\text{Without TR})}$, of the load and actuator for angular shaft position are 180^{o} out of phase and have different magnitudes.

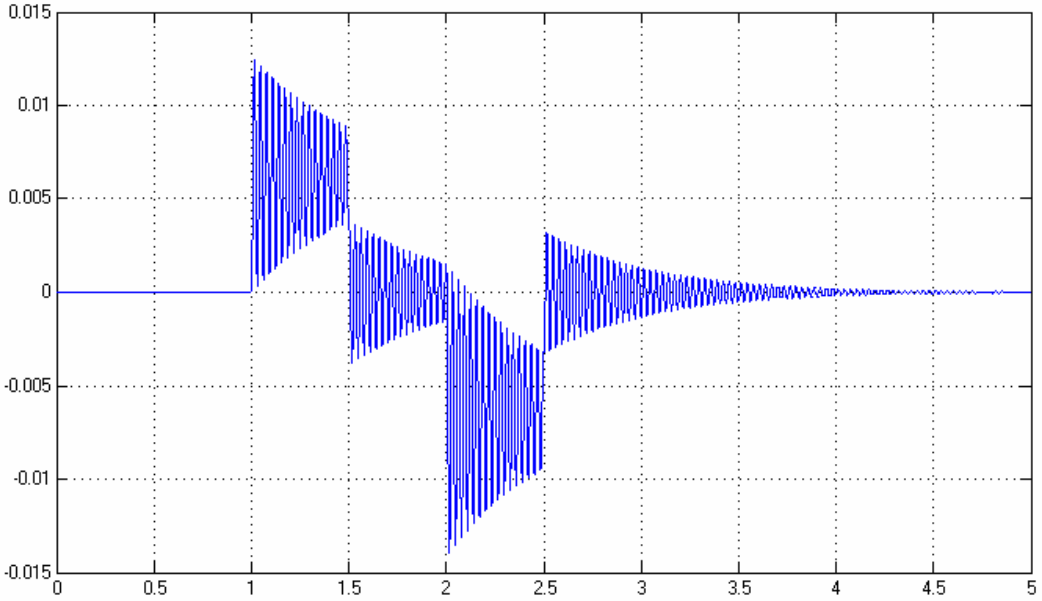

Figure 19: Actuator Shaft Angular Position Error due to Torque Input from Figure 14. Vertical Axis is Magnitude, Horizontal Axis is Time in sec.

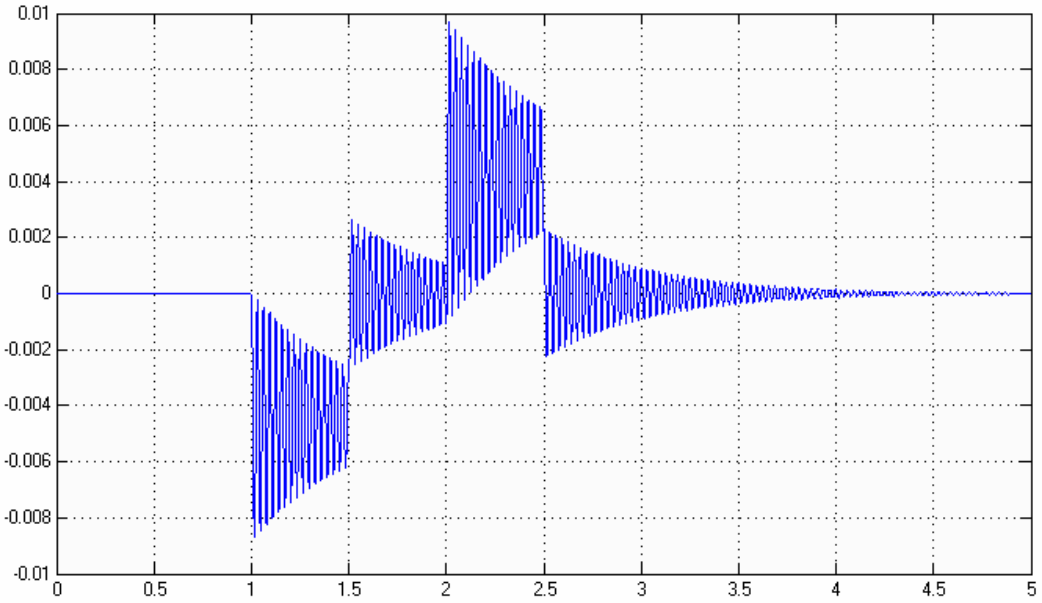

Figure 20: Load Shaft Angular Position Error due to Torque Input from Figure 14. Vertical Axis is Magnitude, Horizontal Axis is Time in sec.

Though it is harder to see the error, $\dot{\theta}_{(\text{With TR})} - \dot{\theta}_{(\text{Without TR})}$, of the actuator and load velocity, Figure 21 and Figure 22 respectively, are also 180° out of phase.

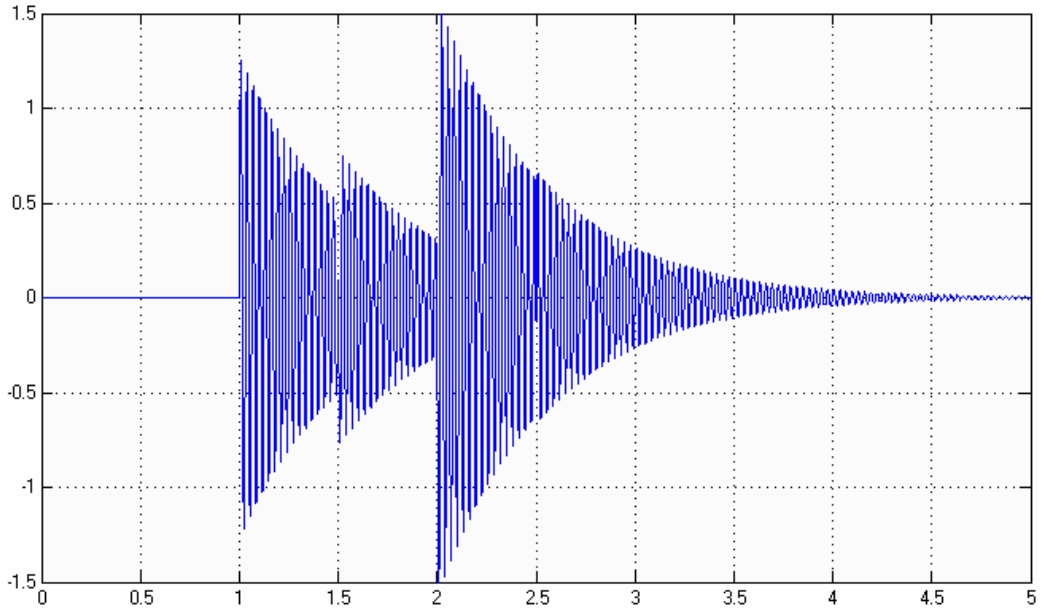

Figure 21: Actuator Shaft Angular Velocity Error due to Torque Input from Figure 14. Vertical Axis is Magnitude, Horizontal Axis is Time in sec.

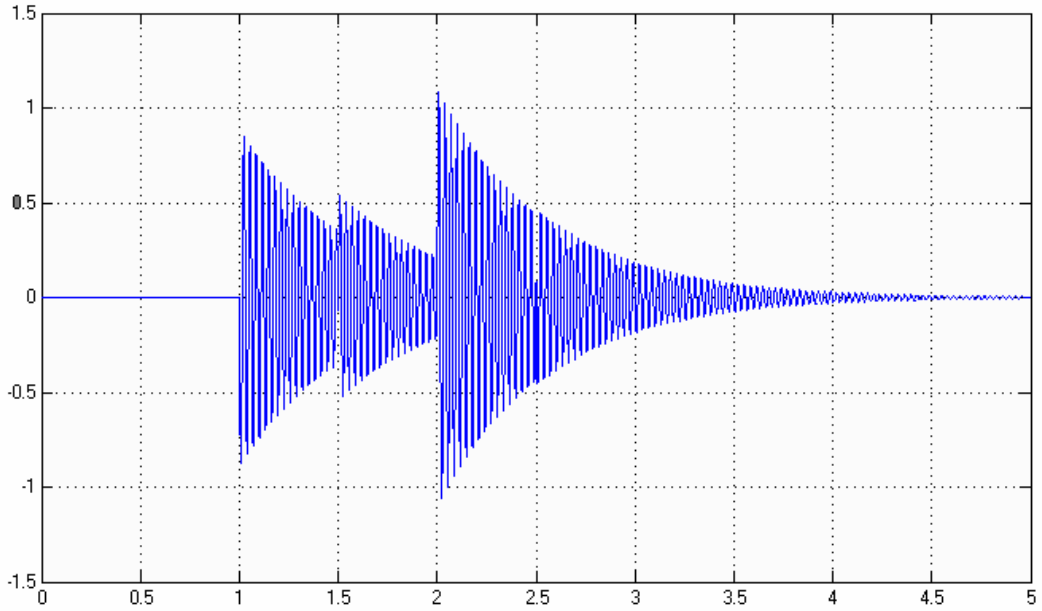

Figure 22: Load Shaft Angular Velocity Error due to Torque Input from Figure 14. Vertical Axis is Magnitude, Horizontal Axis is Time in sec.

j. *Matlab Simulink Model of System with TR and DC Motor Mode acting as Torque Input*

The designs are done using a velocity driven DC motor. The command voltage, is proportional to the open loop velocity. For out models a torque input is needed. Thus the model of a DC motor will need to act as the torque input to the system with TR and the command for the complete system will be the input voltage to the DC motor V_{in}. It is important to note that the current through a DC motor is proportional to the torque applied on its shaft.

Equation 33, Equation 34, and Equation 35 are the dynamic equations for the DC motor used in this experiment. The values listed in Table 2 are the constants for the motor used in the test rig in Appendix F. The remainder of the motor specifications can be found in the motor's data sheet located in Appendix C.

$$\dot{i} = \frac{1}{L}\left(V_{in} - K_e\dot{\theta} - R_a i\right)$$

Equation 33: First Derivative of Motor Current for a DC Motor

$$\ddot{\theta} = \frac{1}{J_a}\left(K_t i - B_a\dot{\theta}\right)$$

Equation 34: Angular Acceleration for a DC Motor

$$\tau = K_t i$$

Equation 35: Output Torque of a DC Motor

Table 2: Values for DC Motor Model from Figure 23

Armature Resistane (Ω)	Armature Inductance (mH)	Voltage Constant (V-sec-rad^{-1})	Torque Constant (N-m-A^{-1})
$R_a = 0.38$	$L = 0.842$	$K_e = 0.042685$	$K_t = 6.046$

Please note that the values stated in Table 2 for the DC Motor in Figure 23 are to be used with the values previously given in Table 1. The values used in Table 2 are from the Pittman Elcom ST N2314 series brushless DC motors [4], see Appendix C for the data sheet.

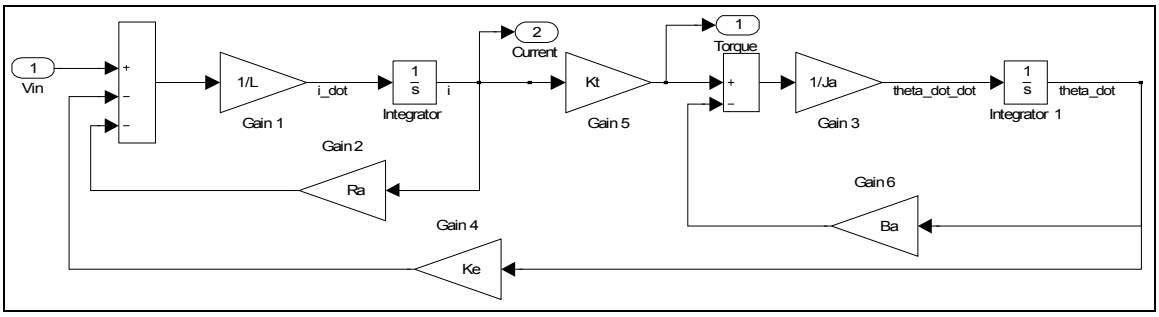

Figure 23: Matlab Simulink Model of a DC Motor from Differential Equation from Equation 33, Equation 34, and Equation 35

The frequency response plot of the DC motor model from Figure 23, with the input being the input voltage and the output being the angular velocity, is located in Figure 24. It is important to note that the break frequency of the motor is more than twice that of the resonant frequency, w_r, of the system with TR from Figure 3.

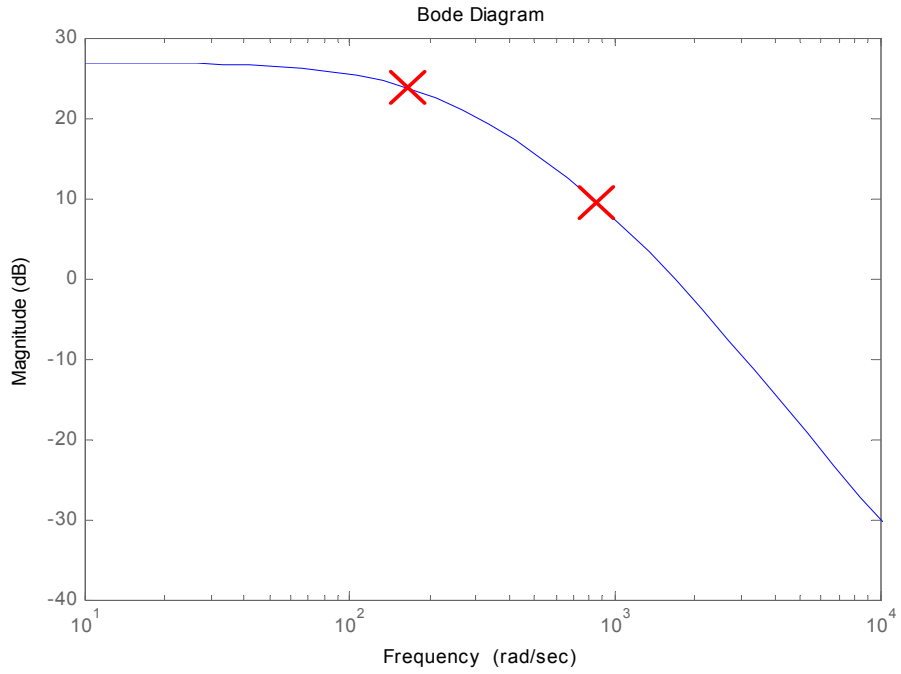

Figure 24: Frequency Response plot of DC Motor Model from Figure 23

Figure 26 shows the system with TR from Figure 11 connected to the DC motor model from Figure 23. Due to the fact that the TR system already contains a portion of the model of the DC motor, only the electrical part of the DC motor has to be added. Figure 25 shows the required electrical portion of the DC motor from Figure 23. Note that it feeds the angular velocity of the shaft from the TR block in Figure 11.

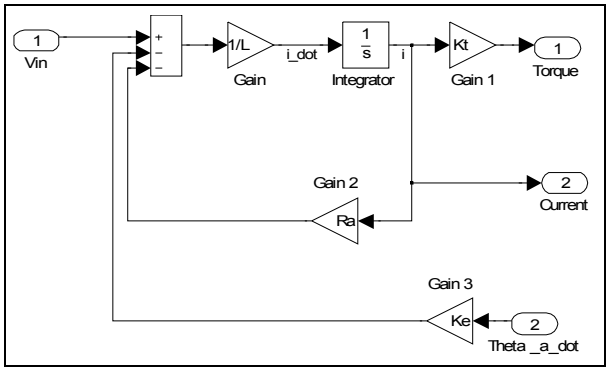

Figure 25: Electrical portion of the DC motor model from Figure 23

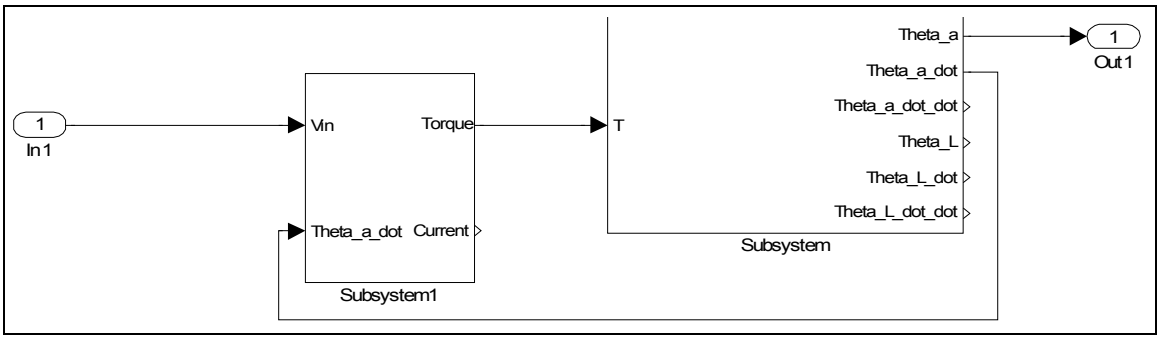

Figure 26: Block diagram of the DC motor model from Figure 25 and the system with TR with torque as the input in Figure 11

The transfer function for the voltage controlled DC motor system with TR in Figure 26 with the actuator's/motor's angular position as the output and the input voltage V_{in} as the input, $\theta_a(s)/V_{in}(s)$, can be found in Equation 36.

$$\frac{\theta_a(s)}{V_{in}(s)} = \frac{3.122E6s^2 + 4.730E6s + 5.203E10}{s^5 + 455s^4 + 1.755E6s^3 + 1.852E7s^2 + 2.221E9s}$$

Equation 36: Transfer function for $\theta_a(s)/V_{in}(s)$, from Figure 26, with parameters from Table 1 and Table 2

k. *Standard Approaches to Designing Control to Reduce the Effects of TR*

Currently industry uses three main methods to reduce the effects of TR in mechanically coupled systems.. The three methods that are used are:

- Reducing the servo's bandwidth so it does not include the TR frequencies. (Appendix E)
- Increasing the couplers spring constant K_c via using higher quality and anti backlash mechanical couplers and gearboxes to push the TR frequencies higher. (Appendix G)
- Using notch filters to reduce the resonant peak. (Appendix D)

The use of stiffer parts/anti-backlash gears is used to increase the spring constant, thus increasing the w_r and w_{ar} frequencies. With the higher w_r and w_{ar} frequencies the useable bandwidth of the system is increased. The drawback to this is that stiffer parts/anti-backlash gears are often much more expensive to purchase. In many instances the latter parts are much stronger than what is needed for the specifications of the system [1].

The most basic method of reducing the problem of TR is reducing the bandwidth of the system so you do not excite the system's TR frequencies. This method works but requires the closed loop system to be slower than that of the TR frequencies. A low pass filter is also often used when reducing the bandwidth of the input to a system with TR. By adding a low pass filter it will ensure that any step input will not excite the TR frequencies. This can also add phase lag and affect the stability.

The use of notch filters is also a method to reduce TR in mechanically coupled systems. When using notch filters in a system with TR a frequency band extending from slightly before the w_r to slightly after the w_r is greatly reduced by the notch filter basically removing it from the control bandwidth. This is the same method used to reduce the 60Hz hum in audio caused by the 60Hz AC power present in most United States Homes. With the absence of these frequencies the system can now operate at much higher bandwidths, past that of w_r. This method is not robust because the frequencies of the TR changes when the load changes, damping changes, etc. Furthermore, notch filters also do not fix the issue of the acting inertial load changing before the w_{ar} to after the w_r as seen in Figure 8.

II. Reduction of the Effects of TR via the use of Resonance Equalization (RE)

a. *Background*

State-variable-feedback (SVF) is a control method that uses different states of a system, such as position, velocity, and acceleration, to create an input to achieve a desired performance. In this case the states of the system consist of the angular position, angular velocity, and angular acceleration with the input being torque. At this point it is pertinent to note the torque applied by a direct current (DC) motor is directly proportional to the current through the windings of the motor. It is also pertinent to note that it is widely known that the DC motor is a fully observable system when the output is the angular position, thus a full or partial state observer can be made for this system. With the latter being said V. Rizzo and W. J. Bigley analyzed what the effects of TR had on various parameters of the system including shaft velocity and input current, Figure 27 is an example of some of these plots.

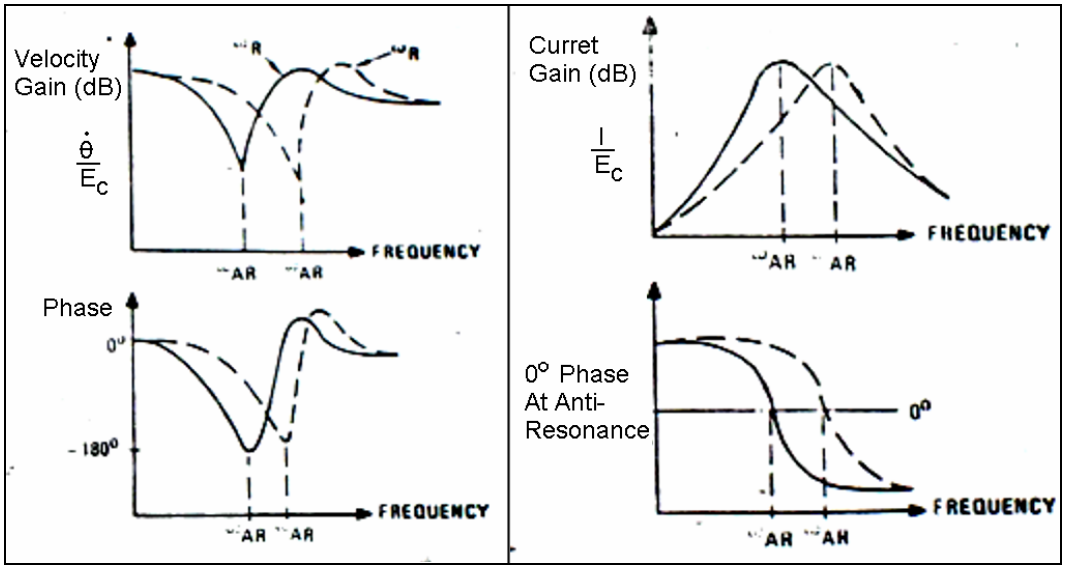

Figure 27: Plot of the Actuator Shaft Velocity and Phase (Left), Plot of the Actuator Current and Phase (Right) around w_r and w_{ar} [1]

Figure 27 shows the plot of the actuator shaft velocity vs. input frequency, and the actuator input current vs. input frequency around the resonance frequencies. Note that the input current and output velocity are almost exactly 180^o out of phase from one another. The importance of this is that the actuator shaft velocity can be used as feedback in combination with the input current to compensate for the effects of the

resonance. The latter relationship will ensure that the control is effective for changes in the resonant frequencies.

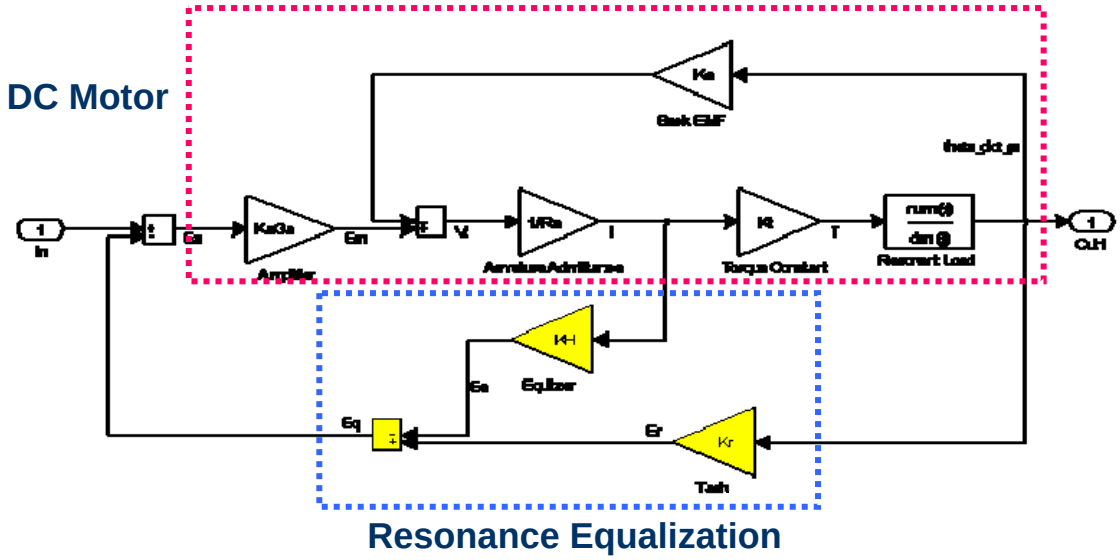

Figure 28: V.Rizzo's Resonance Equalized Rate Loop Diagram [1]

By using the knowledge that the current, or torque, is about 180^{o} out of phase with the angular velocity of the actuator V. Rizzo showed in his paper, [1], that "the resonance peaking factor F is completely eliminated." V.Rizzo's method is implemented in Figure 29 with the SVF gains of -0.2 for the current feedback gain and 20 for the angular velocity feedback. Figure 30 shows the frequency response plot of the system with TR and the addition of V.Rizzo's resonance equalization [1]. When compared to the frequency response of the system with out V.Rizzo's feedback, Figure 6, you will note that there is a decrease in magnitude of the peak and dip at the w_r and w_{ar} of about 63dB. The system with out V.Rizzo's feedback had a peak to dip magnitude of about 64.15dB and the system with V.Rizzo's feedback had a magnitude of about 1.0dB. This also shows a significant increase in the gain margin.

Figure 28 shows the diagram for V.Rizzo's resonance equalized rate loop. The latter rate loop is what has been realized in Figure 29.

It is also important to note that the phase does not change by 180^o thus it is shown that the system will not go unstable under closed loop control due to the phase change. This can be seen by the phase graph of Figure 30. The gain margin is also significantly increased at resonance as seen in the magnitude graph of Figure 30. The use of Matlab's function linmod() confirms for us that the system has increased it's order by two, now it is a sixth order system. The transfer function of $\theta_a(s)/T(s)$, using the values for the TR system and DC motor from Table 1 and Table 2, with V.Rizzo's method using SVF can be found in Equation 37.

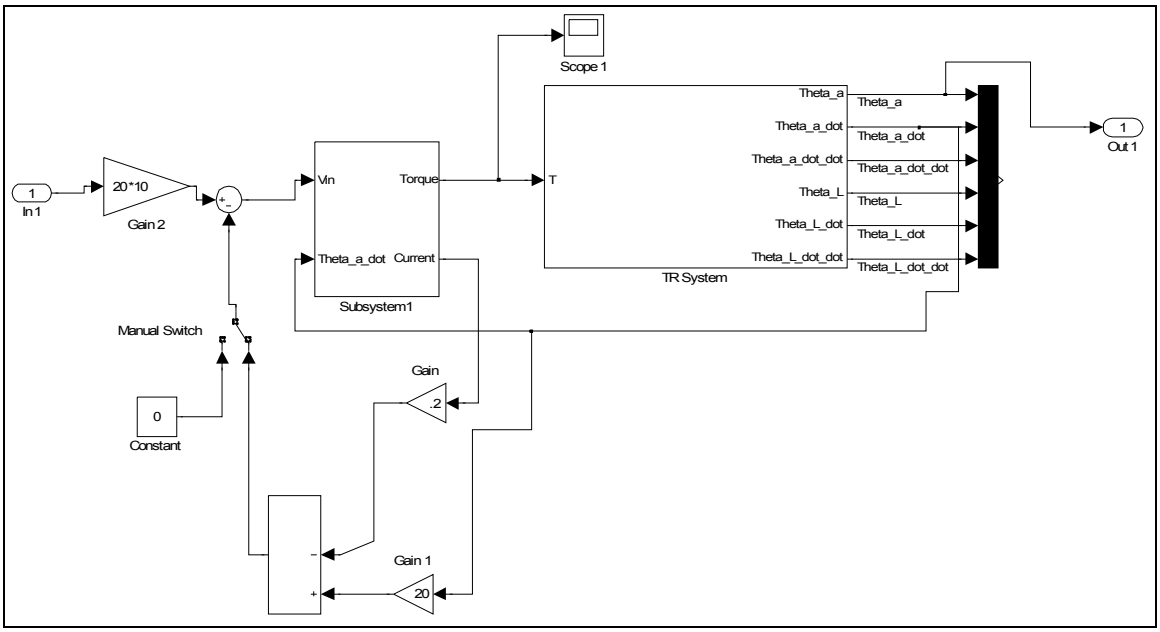

Figure 29: State-Variable-Feedback using V.Rizzo's paper [1] on the System with TR from Figure 3 with the parameters from Table 1 and Table 2

$$\frac{\theta_a(s)}{T(s)} = \frac{6.244E8s^2 + 9.461E8s + 1.041E16}{s^5 + 217.5s^4 + 6.261E7s^3 + 1.035E8s^2 + 1.043E12s^2}$$

Equation 37: Transfer function of system using Rizzo's SVF method from Figure 29

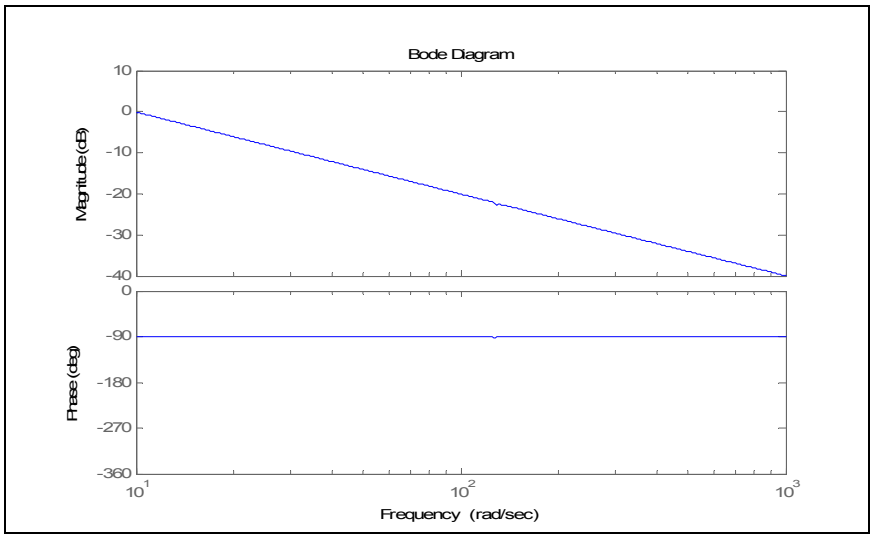

Figure 30: Frequency Response of System with TR and V.Rizzo's [1] SVF Resonance Equalization implemented from Figure 29

Table 3 is a table of the ratio of J_L:J_a and the corresponding properties including:

●Magnitude change around TR.

●Phase change around TR.

●Gain margin.

●Change in dB due to change in effective load as seen in Figure 8 for the closed loop system using Rizzo's SVF.

● Change in dB due to change in effective load for the open loop system.

●Anti-resonant frequency, w_{ar}, in rad/sec.

●Resonant frequency, w_r, in rad/sec.

Ratio (JL:Ja)	Ja oz-in-sec^2	JL oz-in-sec^2	Kc oz/in	TR Mag Change (dB)	TR Phase Change (deg)	ΔdB TE (dB)	ΔdB Open Loop (dB)	W_{ar} rad/sec	W_r rad/sec
100	0.0023	0.23	55	12.53	82.1	0	40.1	15.5	155.4
10	0.0023	0.023	55	2.5	18.2	0.4	20.8	48.9	162.2
2	0.0023	0.0046	55	0.4	4.6	0.5	9.5	109.3	189.4
1.435	0.0023	0.0033	55	0.2	3.5	0.3	7.7	129.1	201.4
0.5	0.0023	0.00115	55	0.1	1.6	0.5	3.5	218.7	267.8
0.1	0.0023	0.00023	55	0	0.3	0	0.8	489.0	512.9
0.01	0.0023	0.000023	55	0	0.1	0	0.1	1546.4	1554.1

Table 3: Table of the ratios of J_L:J_a and their corresponding properties with Rizzo's control

Each row in Table 3 show the results of a separate simulation with a different ratio of the load inertia to the actuator inertia, J_L:J_a. For these experiments the actuator inertia, J_a, was kept constant at 0.0023 oz-in-sec^2, the coupler spring constant, K_c, was also kept constant at 55 oz/in. The load inertia was varied from $0.01 \cdot J_a$ to $100 \cdot J_a$.

a. Resonance Equalization Conclusion

When examining Table 3 it is noted that Rizzo's SVF method is effective in reducing the effects of TR for J_L:J_a ratios of less than two. This method is effective in reducing the change in effective load, i.e. ΔdB, by about a factor of 10 for most values of J_L:J_a of 2 or less, as well as increases the gain margin of the system. Please note that RE requires $\dot{\theta}_a$ and i_a (current through the motor) for proper control.

III. Reduction of TR Via the use of Sliding Mode Control (SMC)

a. *Background*

Sliding Mode Control (SMC) is a form of non-linear control that is able deal with systems that are not linear as well as systems that have parameters which are not precisely known. The main idea about SMC is that the performance of a system is guaranteed to be inside u and x, see Figure 31, within a given error φ and ε respectively. When using SMC one, or multiple, parameters are chosen to be unknown. These *unknown* parameters are specified a range at which the given parameters are able to vary between and still have the system perform within its given bounds φ and ε. It is important to note that this range affects the boundary condition φ and ε. Once the system has entered within the boundary layer, or sliding boundary, it will never leave it. The latter will hold true as long as the parameters which are able to vary do not go out of the designed bounds [5][6].

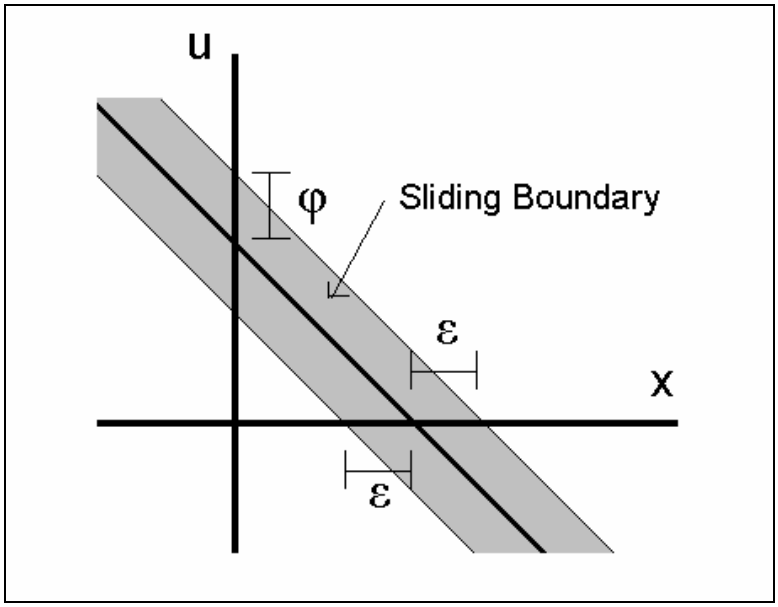

Figure 31: SMC Sliding Boundary/Sliding Layer

The fact that a parameter can be defined to be between a given bound and still have stable control is one of SMC's strongest arguments for it's use for the the reduction of TR. This is also because an exact model of the system does not have to be made for SMC to be effective. SMC is able to take care of some of the un-modeled dynamics including TR. Figure 8 shows the effective inertial load on a system with TR before w_{ar}

and after w_r. As stated previously in Figure 8 and Equation 29 there is an offset in the magnitude of the frequency response due to the change in the effective load. Due to the latter the inertia has been chosen to be the parameter to be unknown within a given bound. The inertial load will vary from $0.9J_a$ to $1.1(J_a+J_L)$ to ensure the system will always fall within the bounds of the SMC and thus stay within the sliding boundary.

The effective load has been taken care of by letting it vary; thus the model of the TR system from Figure 3 and Figure 4 can be reduced and assumed to be a system with out TR.

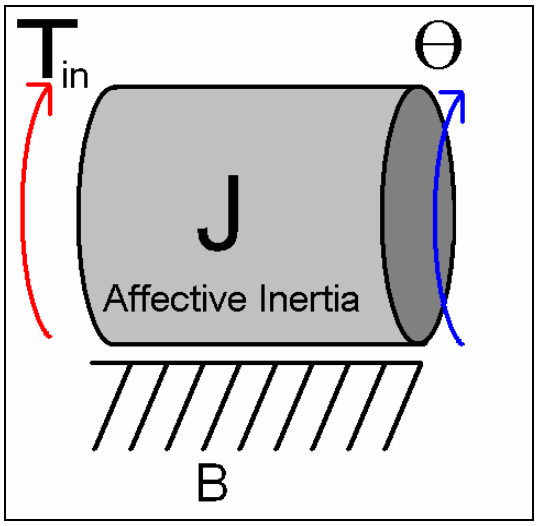

Figure 32: Physical Diagram of Reduced System for SMC

b. *Sliding Mode Control Calculation*

The simplified model in Figure 32 will be used to calculate the control for the SMC then the simulated model will be replaced by the system with TR from Figure 3. Figure 33 is the mechanical network for the system from Figure 32.

Equation 38 through Equation 56 contains the calculations for the SMC input. Please note that the control input for the SMC can be found in Equation 56.

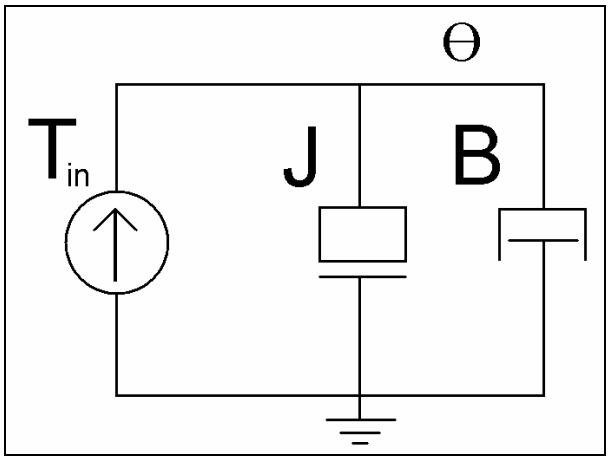

Figure 33: Mechanical Schematic Drawling of Reduced System for SMC based on Figure 3

$$T(t) = J\ddot{\theta} + B\dot{\theta}$$

Equation 38: Differential Equation from System in Figure 33

$$\ddot{\theta} = \frac{1}{J}T(t) - \frac{B}{J}\dot{\theta}$$

Equation 39: Solve for Angular Acceleration from Equation 38

$$\ddot{\theta} = bT(t) - R\dot{\theta}$$

$$b = \frac{1}{J} \quad R = \frac{B}{J}$$

Equation 40: Redefine Parameters from Equation 39

$$J_a \le J \le \left(J_a + J_L\right)$$

Equation 41: Bounds on the effective inertia J

$$R_{\min} \le R \le R_{\max} \qquad R_{\min} = \frac{B}{J_a + J_L} \qquad R_{\max} = \frac{B}{J_a}$$

Equation 42: Bounds on R

$$R_x = \left|R_{\max} - R_{\min}\right|$$

Equation 43: Maximum Deviation of R

$$R_{ave} = \frac{1}{2}\left(R_{\max} + R_{\min}\right)$$

Equation 44: Average R

$$f = -R\dot{\theta}$$

Equation 45: Actual Value of f

$$\hat{f} = -R_{ave}\dot{\theta}$$

Equation 46: Estimated f

$$F \geq \left| f - \hat{f} \right| \qquad \rightarrow \qquad F = R_x \left|\dot{\theta}\right|$$

Equation 47: Solve for F

$$b_{\min} \leq b \leq b_{\max} \quad b_{\min} = \frac{1}{J_a + J_L} \quad b_{\max} = \frac{1}{J_a}$$

Equation 48: Max and Min on b

$$\beta = \left(\frac{b_{\max}}{b_{\min}}\right)^{\frac{1}{2}} = \left(\frac{J_a + J_L}{J_a}\right)^{\frac{1}{2}}$$

Equation 49: Calculation of β with Limitations from Equation 48

$$\hat{b} = \left(b_{\min} b_{\max}\right)^{\frac{1}{2}}$$

Equation 50: Geometric Mean of b

$$s = \dot{\tilde{x}} + \lambda\tilde{x}$$

Equation 51: Define Sliding Surface

$$\dot{\tilde{x}} = \dot{x} - \dot{x}_d$$

$$\tilde{x} = x - x_d$$

Equation 52: Error of Observed States (x) to the Desired State (x_d)

$$\hat{u} = \hat{b}^{-1}\left[\ddot{x}_d - \hat{f} - \lambda\dot{\tilde{x}}\right]$$

Equation 53: Approximation of Continuous Control

It is important to note that λ and η are chosen on a per system basis and will affect the performance and speed of the systems tracking time.

$$u = \hat{u} - Qsign(s)$$

Equation 54: Discontinuous Control to stay on the Sliding Surface

$$Q \geq \hat{b}^{-1}\beta\left(\eta - F\right) + \left(\beta - 1\right)\left|\hat{u}\right|$$

Equation 55: Values of Q sufficiently Large so that it stays on the Sliding Surface

$$u = \hat{b}^{-1}\left[\ddot{x}_d - \hat{f} - \lambda\dot{\tilde{x}}\right] - \left[\hat{b}^{-1}\beta\left(\eta - F\right) + \left(\beta - 1\right)\left|\hat{u}\right|\right] sign(\dot{\tilde{x}} + \lambda\tilde{x})$$

Equation 56: Control Law via Combining Equation 51, Equation 53, and Equation 55 with the control law in Equation 54

Via this implementation of SMC [6] as seen in Chapter III the control input in Equation 56 will give the system a fast and stable response as well as vibration suppression [7].

The values η and λ are restricted by the sampling rate of the controller. Both of the latter values are not to exceed a numerical value of half the sampling frequency in Hz. This simulation has a sampling period of 0.0001sec or 10,000Hz. The values of η and λ can be found in Figure 34.

$$\eta = 0.3$$
$$\lambda = 30,000$$

Figure 34: Chosen Values for η and λ

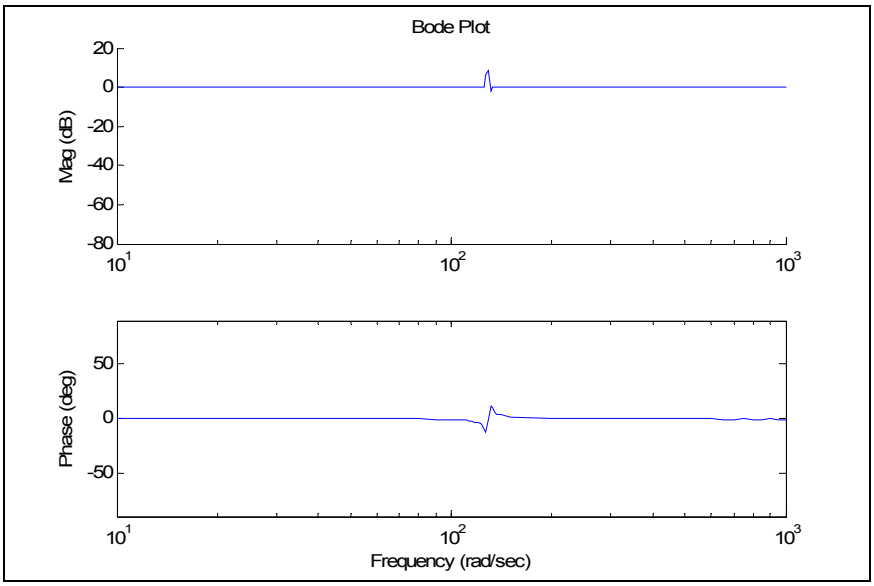

Figure 35: Frequency Response Plot for SMC on System with TR from Figure 3 with η = 0.3 and λ = 30,000

Figure 36 shows the frequency response of the SMC system as shown in Figure 35 except magnified in on the magnitude and phase portions of the plot. From hear it is evident that the magnitude response never peaks above 10dB and the phase shifts no more than ±15°.

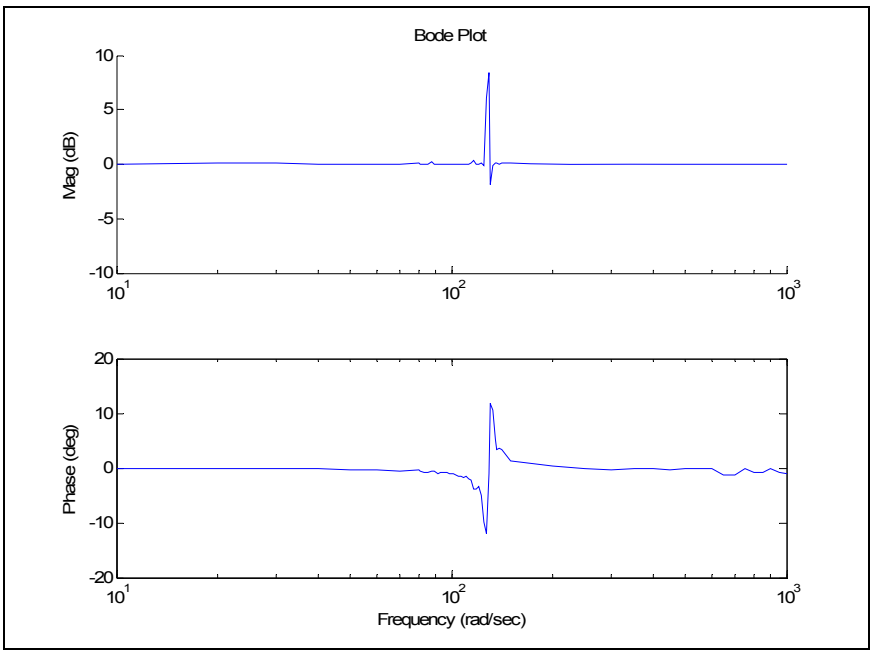

Figure 36: Frequency Response Plot for SMC on System with TR from Figure 3 with η = 0.3 and λ = 30,000 zoomed in on the magnitude and phase

Figure 35 and Figure 36 contain the frequency response plot of the system with TR from Figure 3 and the new control law from Equation 56. It is important to note that the amplitude of the error at resonance is a maximum of 8.4dB and a minimum of negative 1.8dB giving a peak to peak amplitude of about 10.2dB. When compared to the frequency response of the system with TR in Figure 6 it is noted that the peak to peak amplitude of the magnitude at resonance is much greater, at 64.15dB, for the system without resonance equalization than the system with resonance equalization. In addition the phase shift is also reduced to -12.01^o to 11.76^o, at resonance, with an average value of 0^o. The system does not change phase by 180^o over the frequency sweep thus the TR of the system has been reduced and the system is stable with the SMC when acting between these frequencies. It is important to note the 0dB/dec slope of the frequency response plot of the system using SMC was expected because SMC is a closed loop control that makes sure that the first and zero derivative terms track the desired trajectory. Due to the latter we would expect to have a slope of 0dB/dec.

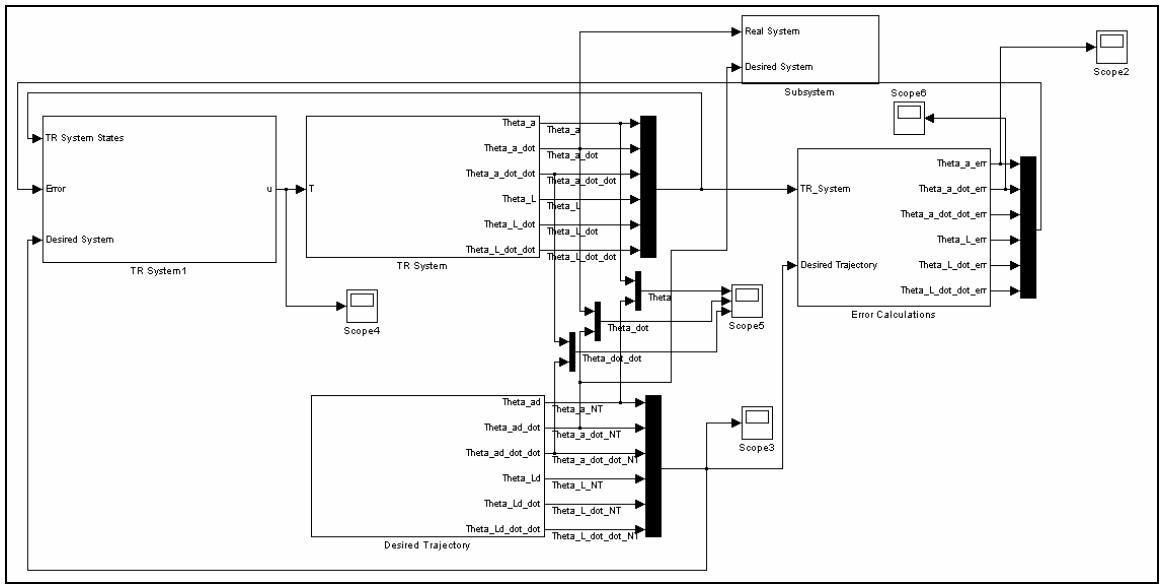

Figure 37: SMC control for Simulink model of system with TR from Figure 3

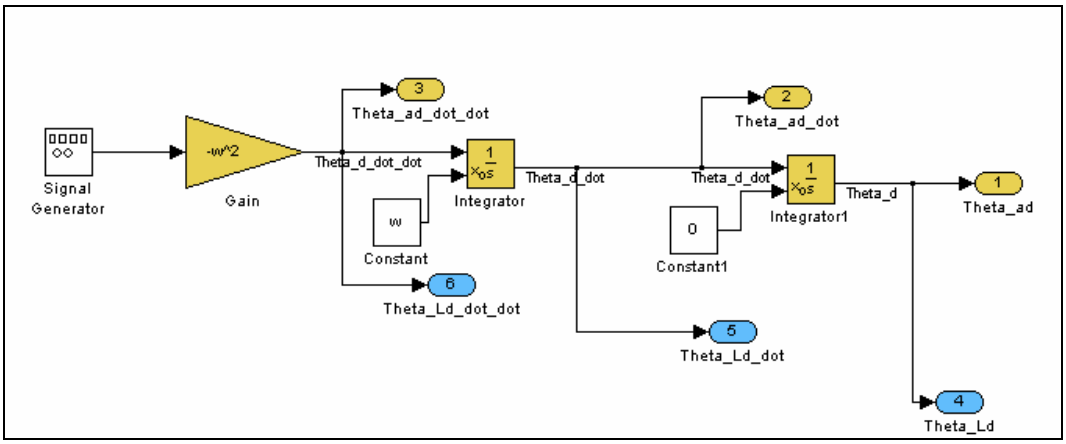

Figure 38: Desired trajectory for SMC where w is the input frequency in rad/sec.

Figure 37, Figure 38, and Figure 39 show the Simulink version of the SMC for the control input from Equation 56.

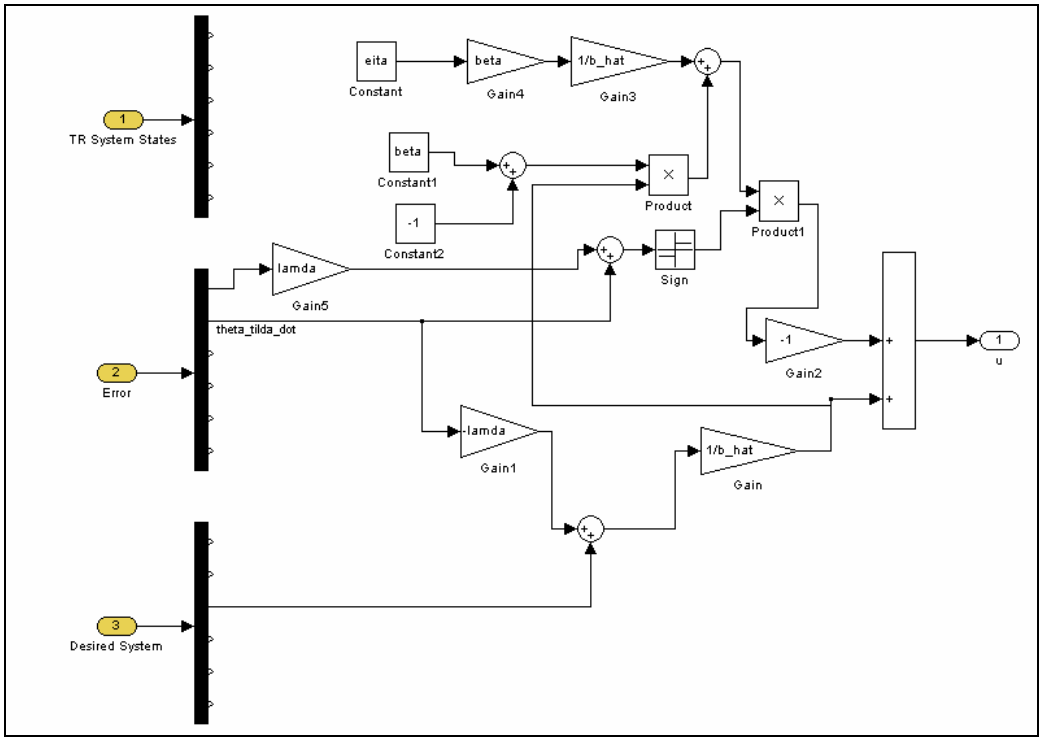

Figure 39: Control law for Figure 37 from Equation 56

Multiple simulations were made on the SMC control method to reduce the effects of TR. Table shows the results of these test for multiple ratios of J_L:J_a.

Ratio (JL:Ja)	J_a oz-in-sec^2	J_L oz-in-sec^2	Kc oz/in	TR Mag Change (dB)	TR Phase Change (deg)	ΔdB (dB)	ΔdB Open Loop (dB)	War rad/sec	Wr rad/sec
2	0.0023	0.0046	55	24.652	130.840	0	9.542	109.346	189.393
1.435	0.0023	0.0033	55	10.200	23.770	0	7.729	129.099	201.444
0.5	0.0023	0.00115	55	0.012	1.815	0	3.522	218.692	267.842

Table 4: Table of ratios of J_L:J_a and their corresponding properties with SMC control

It is apparent from the simulations for multiple ratios of J_L:J_a that when the ratio is below 2 the system will track the desired waveform. When the ratio is further below 2 it is hard to see the TR in the system. It is also important to note that for all of the simulations preformed the closed loop change in dB, as described in Figure 8 and Equation 29, is zero dB. Please note that SMC requires θ_a and $\dot{\theta}_a$ for proper control.

IV. Conclusions

The two different control designs for reducing the effect of TR in coupled systems, RE and SMC, both reduce the effect greatly. Table 5 shows a table that has the results from the control using RE from Table 3 and the control using SMC from Table 4. These results show that RE reduces the TR Mag Change over a greater range than SMC does. However SMC has a ΔdB of 0dB over all of the ratios of J_L:J_a while RE continues to have the switching effect.

Table 5: Effects of changing the ratio J_L:J_a when using RE and SMC

Ratio (JL:Ja)	J_L oz-in-sec^2	ΔdB Open Loop (dB)	ΔdB Closed Loop (dB)	TR Mag Change (dB)	TR Phase Change (deg)	
2.000	0.00460	9.542	0.500	0.400	4.600	RE
1.435	0.00330	7.729	0.300	0.200	3.500	
0.500	0.00115	3.522	0.500	0.100	1.600	
2.000	0.00460	9.542	0.000	24.652	130.840	SMC
1.435	0.00330	7.729	0.000	10.200	23.770	
0.500	0.00115	3.522	0.000	0.012	1.815	

Without Resonance Reduction

With Resonance Reduction

Properties of RE and SMC:

- Resonance Equalization (RE)
  - $\dot{\theta}_a$ and i_a Required
  - Can be used with conventional control methods
  - Works with a wide range of J_L:J_a ratios
  - Highly effective in reducing the TR peak and dips
  - Effective in reducing ΔdB
- Sliding Mode Control (SMC)
  - θ_a and $\dot{\theta}_a$ Required
  - No extra control needed to track desired system
  - No accurate model needed (system can have un-modeled dynamics)
  - Can be used on any coupled system (not limited to mechanically coupled systems)

In conclusion both RE and SMC are effective in reducing the effects of TR in coupled system. RE requires the $\dot{\theta}_a$ and the i_a state to run property. $\dot{\theta}_a$ is a relatively easy to measure state, and thus is usually measured directly. However i_a is not an easy measured state; it normally need to be found via the use of a full or partial order observer. If the controller has the ability to measure both $\dot{\theta}_a$ and i_a, or have the ability to calculate i_a using an observer which requires more computer power, then the use of RE is the preferable choice to reduce the effect of TR in coupled systems. However if i_a is not able to be measured or calculated and θ_a and $\dot{\theta}_a$ are then SMC would be the proper choice. SMC would also be the proper choice of methods to reduce the effects of TR in coupled systems if the coupled system was not a mechanical system but another type of coupled system such as a communications line.

If the system is a mechanically coupled system and the states $\dot{\theta}_a$ and i_a can be measured or calculated then RE should be used. However if any of the latter criteria are not true then SMC should be used.

V. List of References

1. W.J. Bigley; V Rizzo. *Resonance Equalization in Feedback Control Systems*: An ASME Publication, 78-WA/DSC-24, 1978. [15]

2. Nise, Norman S. *Control Systems Engineering Fourth Edition*: John Wiley and Sons INC, 2004

3. Chen, Chi-Tsong. *Linear System Theory and Design Third Edition*: Oxford University Press, New York Oxford, 1999.

4. Ametek: Technical and Industrial Products. *Pittman Elcom ST N2314 Series Brushless DC Servo Motor*. Datasheet, www.ametektip.com.

5. Kwatny, Harry G; Blankenship, Gilmer L. *Nonlinear Control and Analytical Mechanics - A Computational Approach*: Birkhauser, Birkhauser Boston, 2000.

6. Li, Weiping; Slotine, Jean-Jacques E. *Applied Nonlinear Control Third Edition*: Prentice Hall, 2001.

7. Korondi, Peter; Hashimoto, Hideki; Utkin, Vadim. *Direct Torsion Control of Felexible Shaft in an Observer-Based Discrete-Time Sliding Mode*: IEEE Transaction on Industrial Electronics Vol. 45, No. 2, April 1998.

8. 80/20 Inc. *80/20 1"x 1"x L Rods*. http://www.8020.net/, Columbia City, IN. 2008-02-23.

9. US Digital. *E6S-2500-375-HIM3 Quadrature Optical Encoder 2500CPR*. Vancouver, Washington. 2008-01-20.

10. US Digital. *E5S-1024-315-IG Quadrature Optical Encoder 1024CPR*. Vancouver, Washington. 2008-01-20.

11. US Digital. *AD4-B-S RS232 Quadrature Encoder Reader*. Vancouver, Washington. 2008-01-20.

12. xPC. *xPC Target 3.3 Real-Time Hardware in the Loop Solutions*. The MathWorks Inc, Novi, MI. http://www.mathworks.com/products/xpctarget/, 2007-11-12.

13. MicroMo Electronics, Faulharber Group. *MVP 2001A01+ MOD2527 Single Axis Intelligent Drive with Integrated PWM Amplifier RS232C Communication*. Clearwater, FL. http://www.micromo.com/, 2007-09-21.

14. Chmielewski, Tom. *Private Conversation.* 2008

15. Rizzo, Jincent J; Bigley, William J Jr; US Patent Number 4295081. Lockheed electronics Co. Inc. Plainfield NJ. App No: 05/866,394. Filed January 6, 1978.

Appendix A: Transfer Function of θ_L/T Calculation

$$T(s) = (s^2 J_a + sB_a + K_c + sB_c)\theta_a - (K_c + sB_c)\theta_L$$

Equation 57: Laplace Transformation of Equation 1

$$0 = (s^2 J_L + sB_L + K_c + sB_c)\theta_L - (K_c + sB_c)\theta_a$$

Equation 58: Laplace Transformation of Equation 2

$$\theta_a = \left(\frac{s^2 J_L + sB_a + K_c + sB_c}{K_c + sB_c} \right) \theta_L$$

Equation 59: Solve for θ_a in Equation 58

Equation 60 is an important relationship because it shows the difference between the angle of the actuator and the angle of the load.

$$T(s) = \left(\frac{(s^2 J_a + sB_a + K_c + sB_c)(s^2 J_L + sB_a + K_c + sB_c)}{K_c + sB_c} \right) \theta_L - (K_c + sB_c)\theta_L$$

Equation 60: Combine Equation 57 and Equation 59

$$\frac{\theta_L}{T} = \frac{(K_c + sB_c)}{(s^2 J_a + sB_a + K_c + sB_c)(s^2 J_L + sB_a + K_c + sB_c) - (K_c + sB_c)^2}$$

Equation 61: Solve for θ_L/T from Equation 60

$$\frac{\theta_L}{T} = \frac{\frac{1}{J_a J_L}(K_c + sB_c)}{s^4 + (J_a B_L + B_a J_L + B_c J_a + B_c J_L)\frac{s^3}{J_a J_L} + (K_c J_a + B_a B_L + B_c B_a + K_c J_L + B_c B_L)\frac{s^2}{J_a J_L} + (K_c B_a + K_c B_L)\frac{s}{J_a J_L}}$$

Equation 62: Reduction of Transfer Function θ_L/T from Equation 61 to Monic Polynomial

As expected the characteristic equation for the transfer function $\theta_L(s)/T(s)$ in Equation 62 is the same as that of the characteristic equation for the transfer function $\theta_a(s)/T(s)$ in Equation 10. The two systems have the same characteristic equation, therefore they have the same poles of the system. The difference between

the two latter transfer functions is the zeros. The transfer function $\theta_L(s)/T(s)$ from Equation 62 has a first order numerator, and thus has a single zero while $\theta_a(s)/T(s)$ from Equation 10 has a second order numerator and thus has two zeros. The latter means that the expected frequency response of $\theta_L(s)/T(s)$ from Equation 62 will have a steeper slope that than of $\theta_a(s)/T(s)$ from Equation 10.

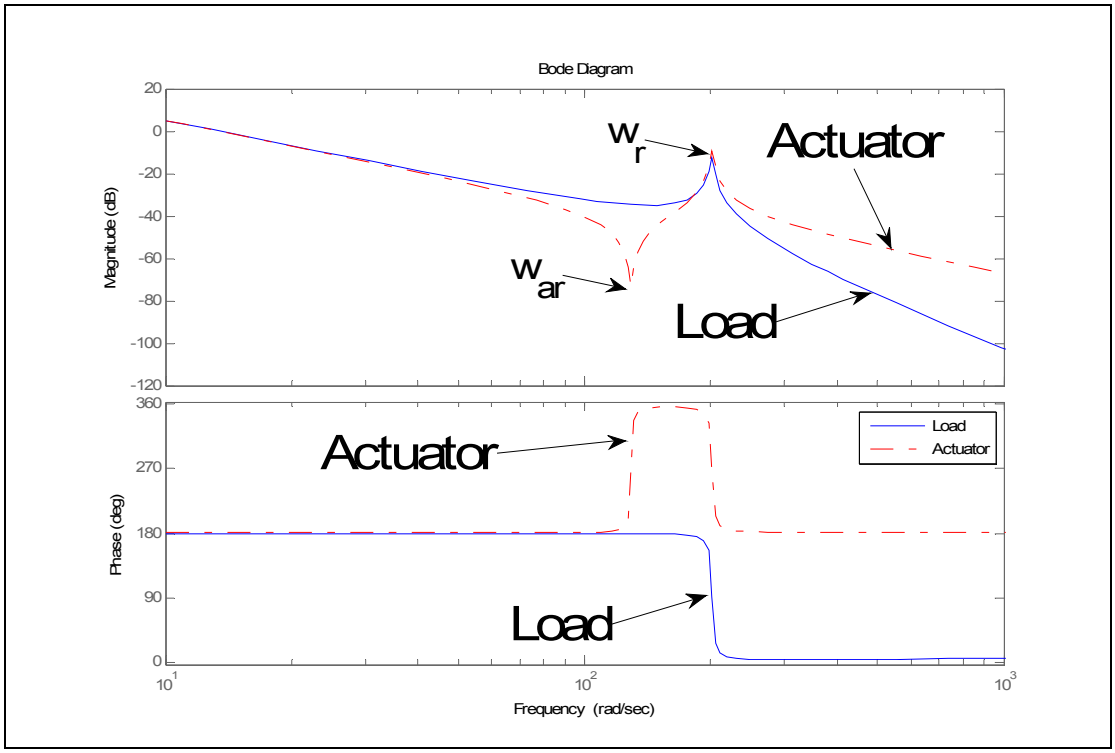

Figure 40: Frequency Response Plot of TR System from Figure 3 with the θ_a and θ_L, Actuator and Load Angle Respectively, as the output.

Figure 40 shows the frequency response plot of the system from Figure 3 with the load and the actuator shaft angles being the outputs. It is important to note that when the frequency response of the system with the torque as the input and the load angle as the output, $\theta_L(s)/T(s)$, and the system with the torque as the input and the actuator angle as the output, $\theta_a(s)/T(s)$, are compared that the two systems act similarly before the resonant and anti-resonant peaks in both the magnitude and phase of the frequency response. Due to the fact that $\theta_L(s)/T(s)$ has one less pole than $\theta_a(s)/T(s)$ after the resonance the $\theta_L(s)/T(s)$ decays at an extra -20dB/dec when compared to $\theta_a(s)/T(s)$. The $\theta_L(s)/T(s)$ system lags in phase by about 180^o after w_r and stays lagging by that amount. $\theta_a(s)/T(s)$ starts to lead in phase by about 180^o after w_{ar} and returns to its original phase after w_r.

It is also interesting to note that there is no apparent effect of the w_{ar} on the frequency response of $\theta_L(s)/T(s)$ on both the magnitude and the phase. In addition $\theta_L(s)/T(s)$ and $\theta_a(s)/T(s)$ have similar magnitude responses to an input around w_r. After w_r the magnitude of the frequency response of $\theta_L(s)/T(s)$ falls off at about -20dB/dec faster than that of $\theta_a(s)/T(s)$.

Appendix B: Effects on the gain margin on a system with added damping

Damping was added to the load and the actuator on the TR system from Figure 3 and compared to that of the system with out damping. The Transfer function of the system with out damping on the load and the actuator is shown in Equation 23 and Equation 63. The transfer function of the TR system with added damping to the actuator and load can be found in Equation 64.

$$\frac{\theta_a(s)}{T(s)} = \frac{434.8s^2 + 658.8s + 7.246E^6}{s^4 + 3.689s^3 + 4.058E^4s^2}$$

Equation 63: Transfer function of system with TR and no damping on the load and actuator with values from Table 1

$$\left.\frac{\theta_a(s)}{T(s)}\right|_{Damping} = \frac{434.8s^2 + 1.383E4s + 7246E6}{s^4 + 65.3s^3 + 4.164E4s^2 + 1.246E6s}$$

Equation 64: Transfer function of system with TR and damping on the load, B_L=0.1 oz-in/krpm and actuator, B_a=0.072 oz-in/krpm, with the remaining values from Table 1

It is important to note that the TR system with no damping, Equation 63, has a double pole at the origin. The addition of damping on the load and on the actuator shifts one of the poles at the origin to the left. Unlike the TR system with no damping on the actuator or load, the TR system with damping is not marginally stable.

The frequency response of both the TR system with no damping and the TR system with damping on the load and on the actuator are plotted in Figure 41. It is important to note that with the added damping the peak at w_r, and the dip at w_{ar}, have both been reduced. In turn the gain margin has been increased to 28.5dB.

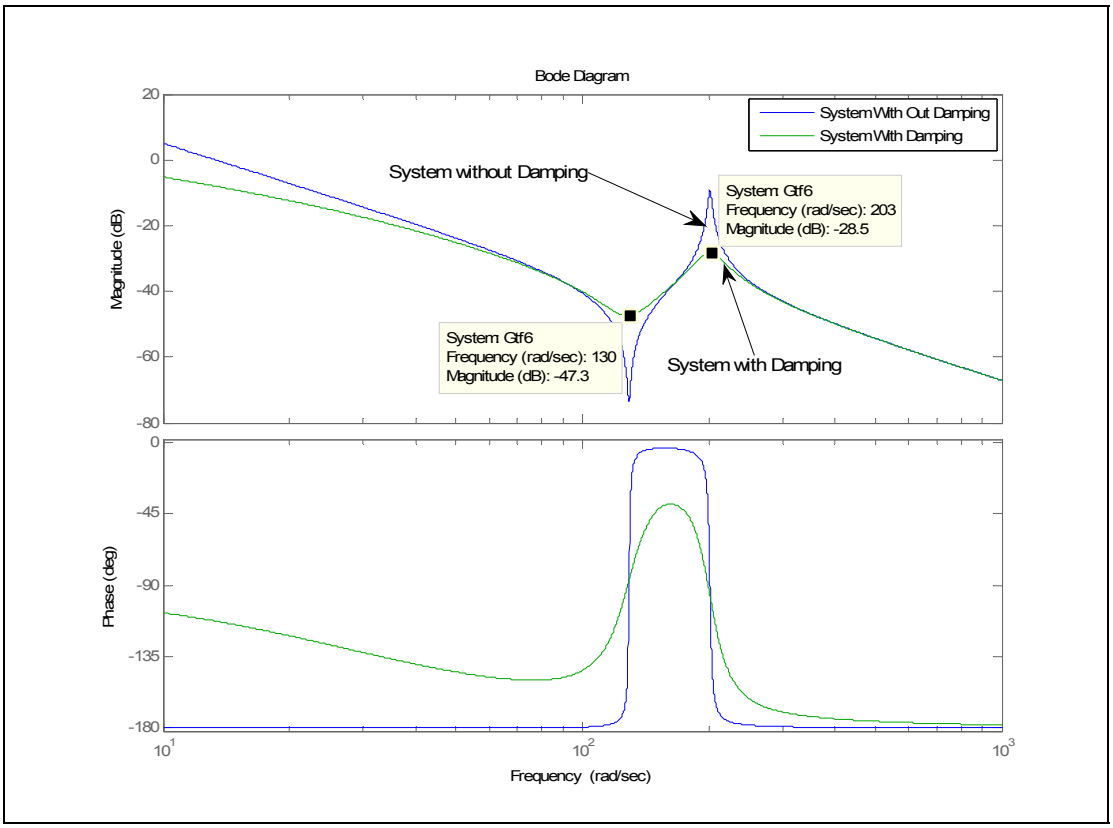

Figure 41: Frequency response plot of TR system with out damping on the actuator and the load, Figure 6, and frequency response of TR system with damping on the actuator, 0.072 oz-in/krpm, and damping on the load of 0.1 oz-in/krpm

Please note that the value for the damping of the actuator was chosen from the data sheet, Appendix C, for the motor which was used for the test rig in Appendix F

Appendix C: Pittman N2314 Series Motor Data Sheet [4]

N2314 SERIES BRUSHLESS DC SERVO MOTOR

PITTMAN

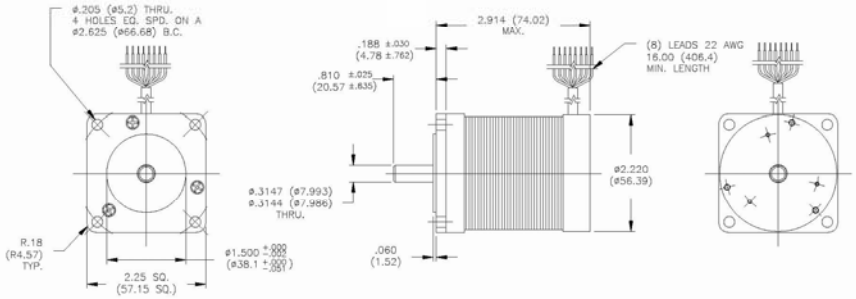

Motor Data	Symbol	Units	Winding Designation							
			15.2 V	19.1 V	24.0 V	30.3 V	38.2 V	48.0 V	60.0 V	76.4 V
Supply Voltage (Reference)	V_e	V	15.2	19.1	24.0	30.3	38.2	48.0	60.6	76.4
Continuous Torque	T_c	oz-in	40	40	40	40	40	40	40	40
		Nm	0.29	0.29	0.29	0.29	0.29	0.29	0.29	0.29
Speed @ Cont. Torque	S_c	rpm	6150	6170	6420	6560	6420	6580	6670	6480
Current @ Cont. Torque	I_c	A	15.9	12.3	9.97	7.97	6.13	4.98	3.99	3.07
Continuous Output Power	$P_{o,c}$	W	184	184	192	196	192	197	199	194
Motor Constant	K_M	oz-in/√W	8.1	8.8	9.1	9.4	9.8	9.8	9.8	10.0
		Nm/√W	0.057	0.062	0.065	0.066	0.069	0.069	0.069	0.071
Torque Constant	K_T	oz-in/A	3.02	3.93	4.84	6.04	7.86	9.67	12.1	15.7
		Nm/A	0.0213	0.0277	0.0341	0.0427	0.0555	0.0683	0.0854	0.1110
Voltage Constant	K_E	V/krpm	2.23	2.91	3.58	4.47	5.81	7.15	8.94	11.62
		V s/rad	0.0213	0.0277	0.0341	0.0427	0.0555	0.0683	0.0854	0.1110
Terminal Resistance	R_{mt}	Ω	0.14	0.20	0.28	0.41	0.65	0.98	1.51	2.45
Inductance	L	mH	0.22	0.37	0.56	0.88	1.49	2.25	3.52	5.95
No-Load Current	I_{nl}	A	0.65	0.50	0.41	0.33	0.25	0.20	0.16	0.12
No-Load Speed	S_{nl}	rpm	6740	6540	6680	6750	6550	6680	6750	6550
Peak Current	I_{pk}	A	109	96.6	85.7	73.3	59.0	49.1	40.1	31.2
Peak Torque	T_{pk}	oz-in	326	378	412	441	462	473	482	488
		Nm	2.30	2.67	2.91	3.11	3.26	3.34	3.41	3.45
Coulomb Friction Torque	T_f	oz-in	1.5	1.5	1.5	1.5	1.5	1.5	1.5	1.5
		Nm	0.011	0.011	0.011	0.011	0.011	0.011	0.011	0.011
Viscous Damping Factor	D	oz-in/krpm	0.072	0.072	0.072	0.072	0.072	0.072	0.072	0.072
		Nm s/rad	4.9E-06	4.9E-06	4.9E-06	4.9E-06	4.9E-06	4.9E-06	4.9E-06	4.9E-06
Electrical Time Constant	τ_e	ms	1.6	1.9	2.0	2.1	2.3	2.3	2.3	2.4
Mechanical Time Constant	τ_m	ms	4.6	3.9	3.6	3.4	3.2	3.2	3.1	3.0
Thermal Time Constant	τ_{th}	min	25	25	25	25	25	25	25	25
Thermal Resistance	R_{th}	°C/W	4.7	4.7	4.7	4.7	4.7	4.7	4.7	4.7
Max. Winding Temperature	θ_{max}	°C	130	130	130	130	130	130	130	130
Rotor Inertia	J_r	oz-in-sec^2	2.1E-03	2.1E-03	2.1E-03	2.1E-03	2.1E-03	2.1E-03	2.1E-03	2.1E-03
		kg m^2	1.5E-05	1.5E-05	1.5E-05	1.5E-05	1.5E-05	1.5E-05	1.5E-05	1.5E-05
Motor Weight (Mass)	w_M	oz	29.4	29.4	29.4	29.4	29.4	29.4	29.4	29.4
		g	832	832	832	832	832	832	832	832

Performance (24 V Winding)

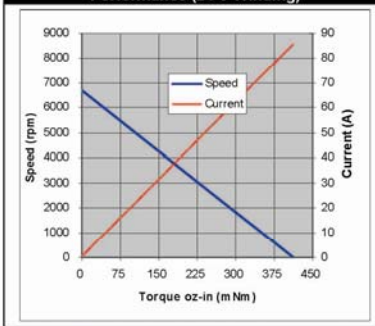

Standard Features

- Shielded Ball Bearings
- 4-Pole Rotor
- Neodymium Magnets
- 3-Phase Stator
- Hall Sensors
- NEMA 23 Mounting

Complementary Products

- G42A Planetary Gearbox
- G42B Planetary Gearbox
- G51A Spur Gearbox
- E35A Optical Encoder
- E30A Optical Encoder
- E60A Optical Encoder
- E30B Optical Encoder
- E60B Optical Encoder

Connection Chart

Color/Pin	Function
Brown	Motor ϕA
Red	Motor ϕB
Orange	Motor ϕC
Grey	Sensor 1
Blue	Sensor 2
White	Sensor 3
Violet	Vcc
Black	Ground

120° Electrical Spacing

Notes:

[1] All values specified at 25°C ambient temperature and without heat sink.

[2] Peak values are theoretical and supplied for reference only.

AMETEK TECHNICAL & INDUSTRIAL PRODUCTS

215-256-6601 (USA) • +39 0373 210245 (Europe) • (86-21) 6426 8111 ext 47 (Asia)

www.ametektip.com

Appendix D: Reducing TR via the use of notch filters

Figure 42 shows the block diagram of the system with TR from Equation 23 in a closed loop system with unity feedback on the angle of the actuator, θ_a, a proportional gain of 0.3 and a notch filter centered on w_r with a width of ±4% of w_r. The notch filter will reduce the amplitude of the response at the resonant frequency w_r.

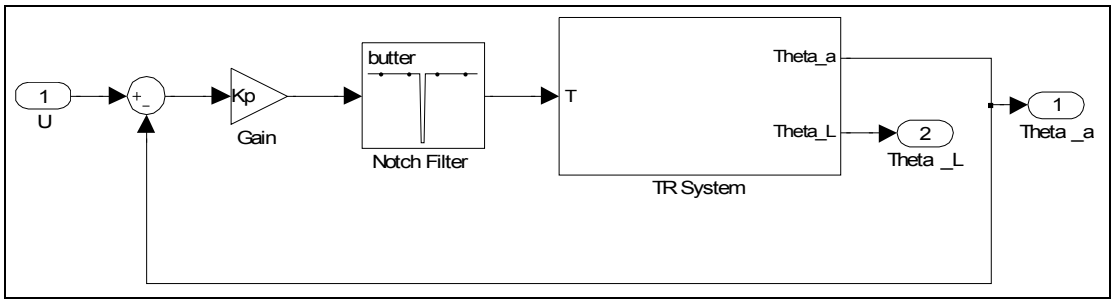

Figure 42: Unity gain closed loop TR system with proportional gain of 0.3 and a notch filter around w_r ±4%

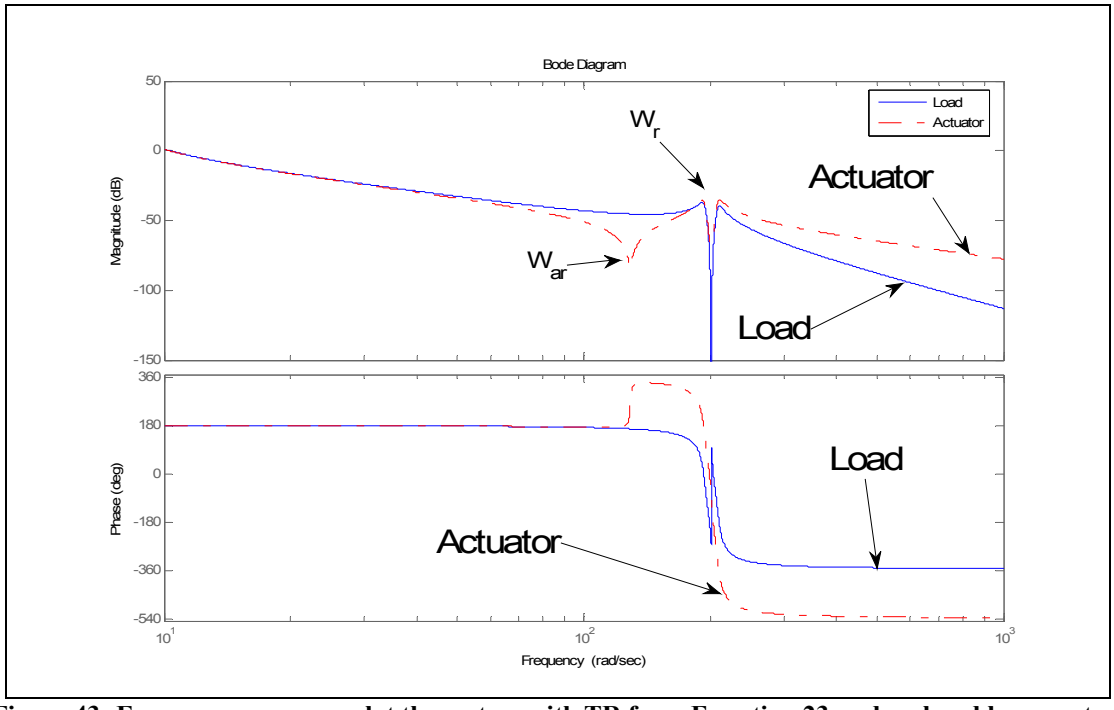

Figure 43: Frequency response plot the system with TR from Equation 23 under closed loop control from Figure 42

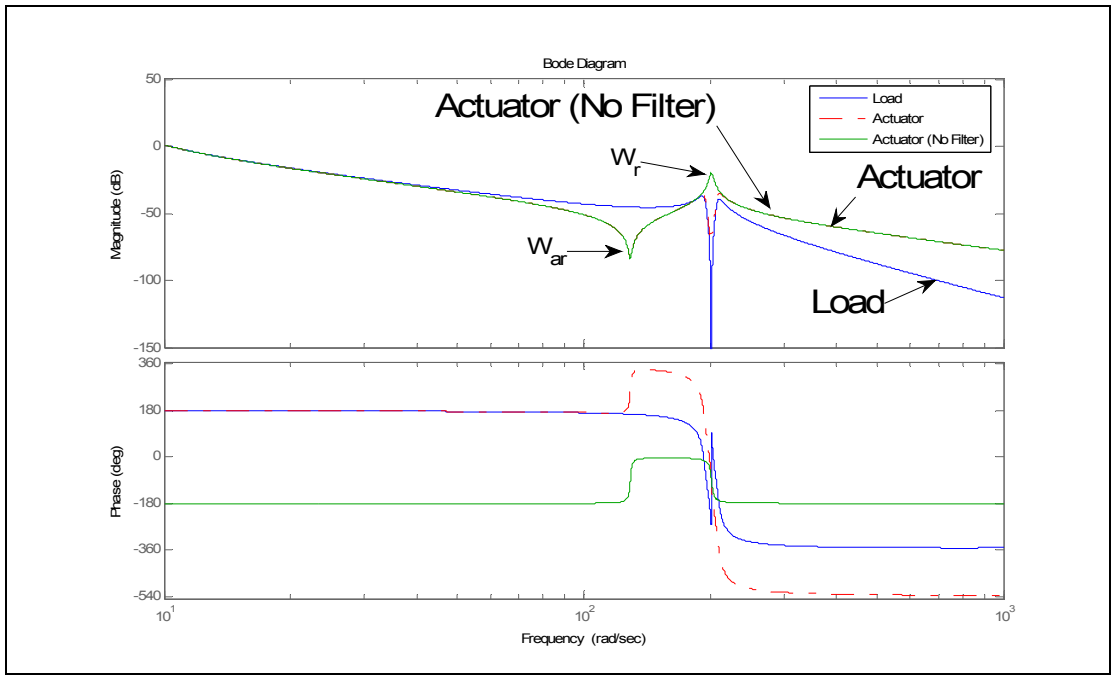

Figure 44: Frequency response plot the system with TR from Equation 23 under closed loop control from Figure 42 with the frequency response of the same system barring the notch filter

Figure 43 and Figure 44 shows the frequency response of the closed loop system in Figure 42. In Figure 43 it is shown that the amplitude of the frequency response at resonance is significantly reduced, thus increasing our gain margin. Figure 44 shows how high the peak would have been in this closed loop form if there was no notch filter present. Figure 44 also shows that the notch filter only significantly affects the area around $w_{r,}$ thus it works as designed. Due to the fact that the load is not affected, to a significant extent, by the anti-resonance the use of the notch filter smoothes out the frequency response of the load dramatically.

Appendix E: Reducing TR via the use of reduced bandwidth and low pass filters

Figure 45 shows the block diagram of the system with TR from Equation 23 in a closed loop system with unity feedback on the angle of the actuator, θ_a, a proportional gain of 0.3 and a 4th order low pass filter, LPF, with the break point as the average of w_{ar} and w_r. The LPF is used to make sure no high frequency content excites the TR.

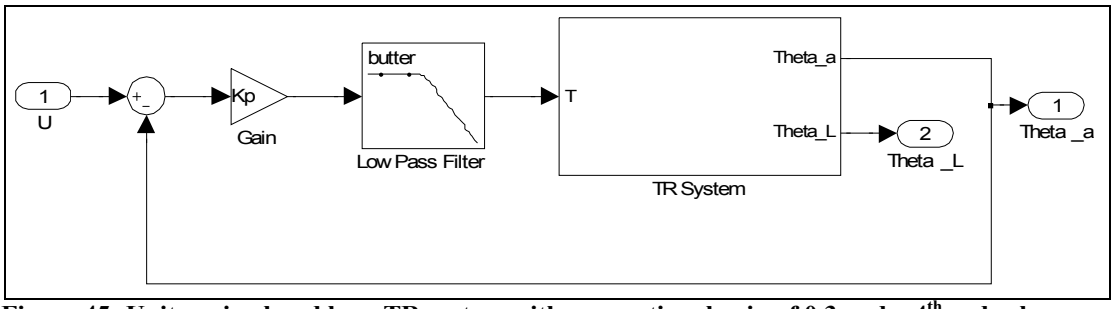

Figure 45: Unity gain closed loop TR system with proportional gain of 0.3 and a 4th order low pass filter

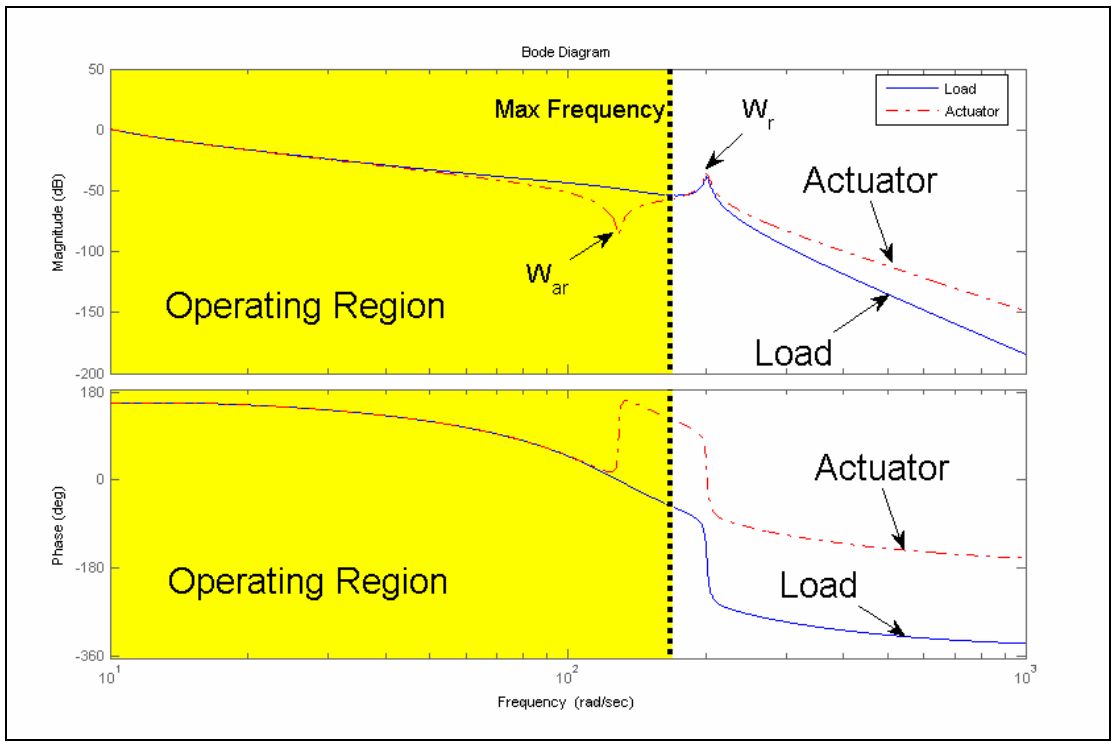

Figure 46: Frequency response plot the system with TR from Equation 23 under closed loop control from Figure 45

Figure 46 shows the frequency response of the closed loop system in Figure 45. The region in Figure 46 to the left of the *Max Frequency* dotted line, denoted in yellow, is the *Operating Region*. In order to ensure that the system is stable the input command must be inside the operating region in respect to the frequency axis. This method is an inexpensive and quick way to reduce the problem of TR. However the speed at which you are able to track an input is reduced.

Appendix F: Design of a Test Rig that Exhibits TR for Testing Different Control Strategies in a Real Time Environment

a. *The Test Rig*

In order to verify the results from Chapter II, V.Rizzo's State Variable Feedback (SVF) method, and Chapter III, Sliding Mode Control (SMC), in the real world a test rig was created. The test rig would allow the user to place the TR at the desired frequency and perform closed loop control in real time. The placement of the TR is done by allowing the user to change the inertia of the load as well as the spring constant of the coupling device. The states, angular position, angular velocity, and angular acceleration, are calculated by quadrature encoder and fed back to a hard real time control system on a computer running xPC. Figure 47 shows the block diagram of how the over all test rig works. The purpose of the test rig is to measure the frequency response of the system with TR with and without the SVF and SMC methods of reducing the effect of TR.

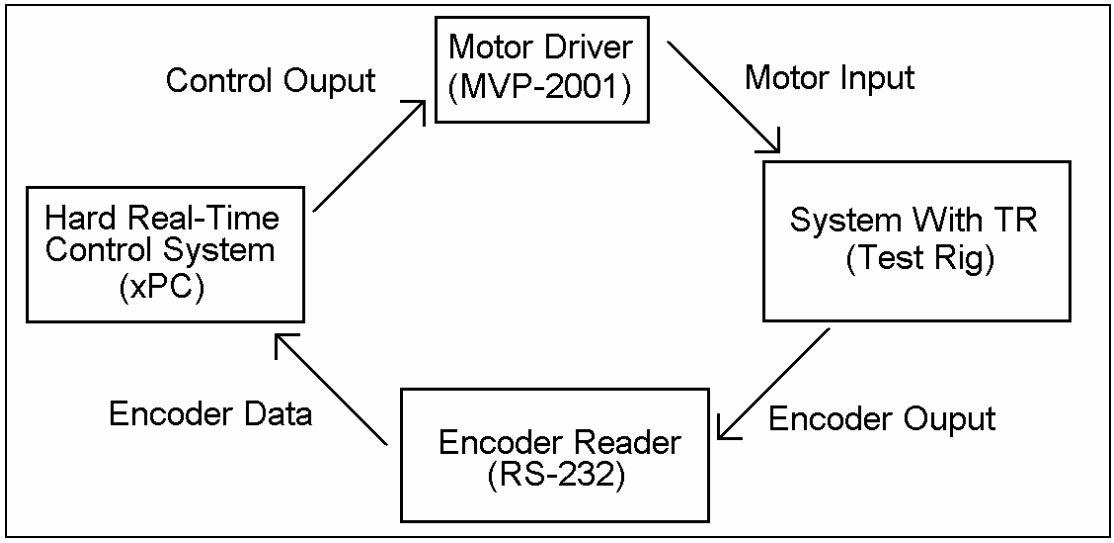

Figure 47: Test Rig Block Diagram

I. Mechanical Setup

The frame of the Test rig is made out of half inch thick aluminum plates and one inch aluminum rods of 80/20 [8]. The heavy aluminum plates were chosen because of the characteristics of the metal. Aluminum is stiff and strong, which gives it an extremely high resonant frequency, relative to that of the TR system,

and it is easily machined. The half inch thick aluminum plates were bolted into a desk. A rubber pad was placed between the main rig and the desk to absorb some of the vibrations. The 80/20 was chosen because it allows for movement of the load and of the motor to accommodate different coupler/belt sizes. Figure 48 is the basic side profile of the test rig setup.

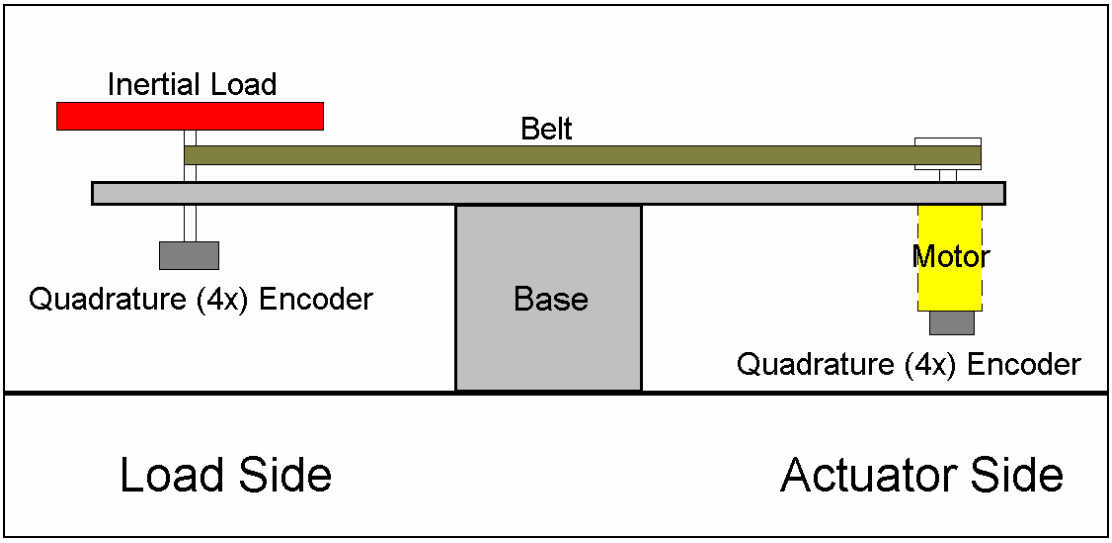

Figure 48: TR Test Rig Diagram

It can be noted from Figure 48 that the inertial load, a disc, is connected to the motor/actuator via a belt. The states of the motor/actuator and the load are measured by quadrature optical encoders. It is important to note that the encoder on the motor/actuator side is measuring the shaft angle of the motor before it goes through the gearbox. If the TR of the gearbox falls within the frequency bandwidth of the test sweep, the effect of the TR in the gearbox would be expected to be picked up by the test rig as well. Figure 49 and Figure 50 shows the over all setup of the mechanical part of the test rig.

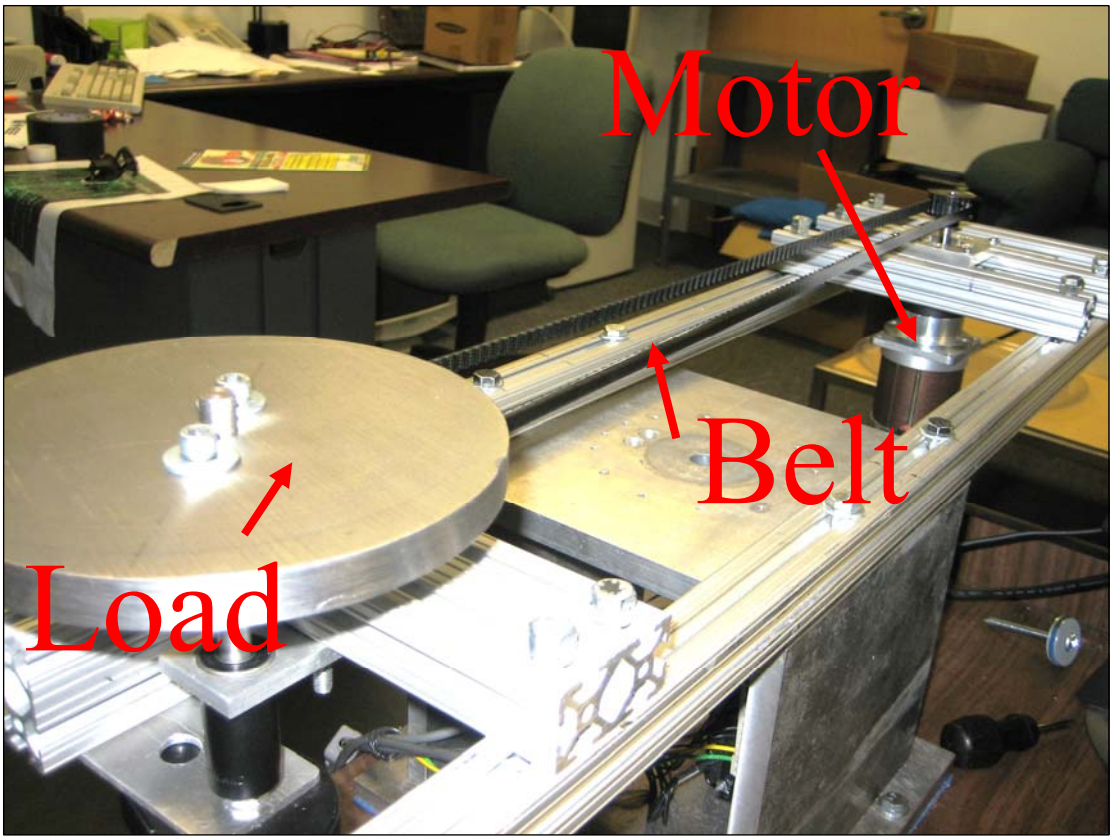

Figure 49: Test Rig. Load (Bottom Left), Belt (Middle), Motor (Top Right)

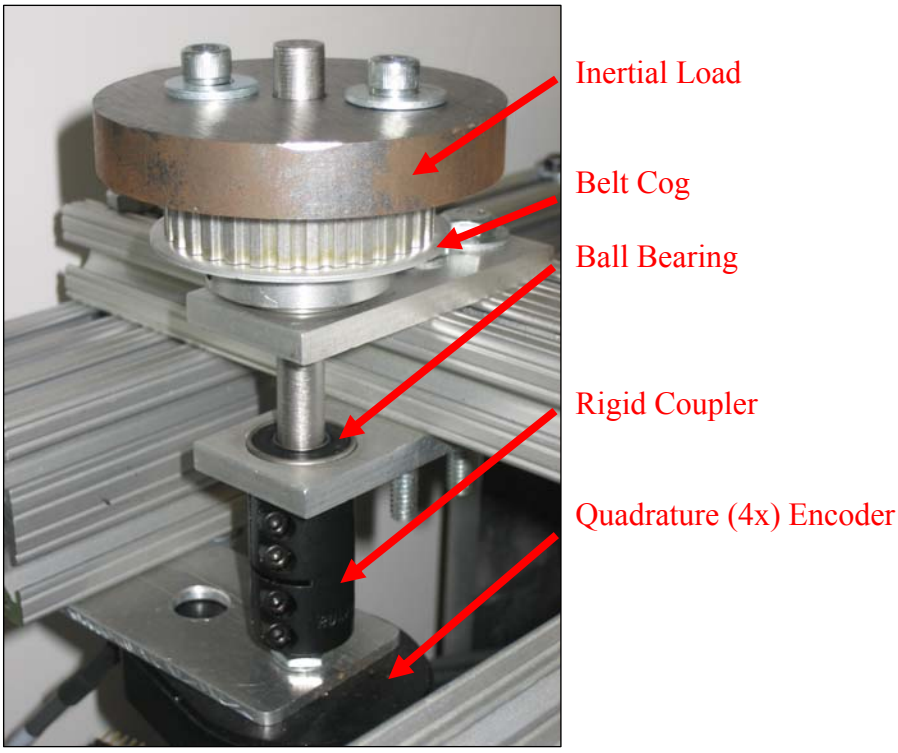

Figure 50: Test Rig Load. Inertial Load (Top), Rigid Coupler (Middle), 4x Encoder (Bottom)

The inertial load, Figure 50, is held in place by two ball bearings and is connected to a 2500 tick quadrature optical encoder [9] via a rigid shaft coupler. The rigid coupler was chosen to ensure no resonance in the test band due that that coupler. The inertial load from Figure 50 can be changed to make the inertia about equal to that of the motor, less than that of the motor, and much greater than that of the motor. Figure 51 shows a few of the inertial discs that can be used with the test rig in Figure 49. The belt cog in Figure 50 connects the belt from the motor to the load. This belt can be made out of any material but must be less than half of an inch wide, a pitch of 0.2", and an outer diameter (OD) less than 72". Belts ranging from 33" to 63" OD and 5/16" wide made of both rubber and urethane were procured for use with this test rig.

Figure 51: Inertial Loads for the Test Rig

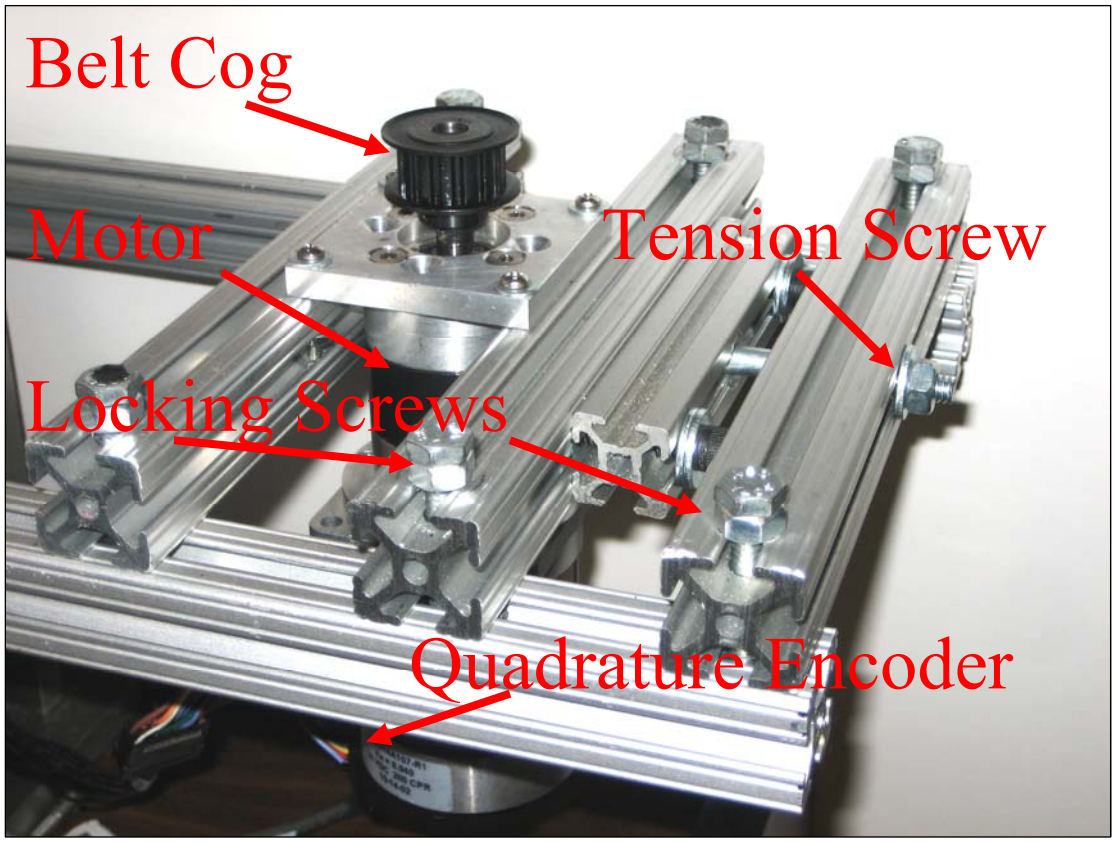

Figure 52: Test Rig Motor Mount and Tension Calibration

The TR depends greatly on the inertial load and the spring constant of the coupler. Figure 51 shows the inertial loads/discs, these loads are constant loads and only a limited amount of inertial discs are available. In order to place the TR in the desired location controlling the spring constant of the coupler is important. The *Tension Screw* from Figure 52 is the device that allows for accurate control of the tension on the belt on the test rig thus accurately controlling the spring constant of the system. Given the ability to pick an inertial load a accurately specify a spring constant the TR is able to be placed in it's desired location in the frequency spectrum.

II. Electrical Setup

The encoder in Figure 52 is an optical quadrature encoder with 1024 CPR [10]. The encoder is located on the armature shaft of the brushless DC [4] before the 6.75:1 ratio gear box. The encoder from the load side, Figure 50, and the encoder from the motor/actuator side, Figure 52, are both read by a RS232 quadrature encoder reader [11]. The information gathered by the encoder reader is then sent to the hard real-time

control system running xPC [12]. The xPC system will process the data gathered from the encoders. It will then output via RS232 the new control data to the MVP2001 [13] single axis intelligent drive being used as a simple brushless motor driver. The input data that xPC sends to the MVP2001 is simply the desired duty cycle, 0-100%, and the desired direction, clockwise or counter clockwise. Please note that this is an open loop command within the MVP2001. Figure 53 is the Simulink/xPC file that controls and reads the information from the test rig shown in Figure 49. The large block in the center of Figure 53 is the main I/O block for the hardware. This block contains the motor command input, scaled to ±24V, and the motor and load angle and velocities as the outputs, in rad and rad/sec respectively. Within the box all of the proper conversions are done to send the data and receive it in units for volts (V), angle (rad), and velocity (rad/sec).

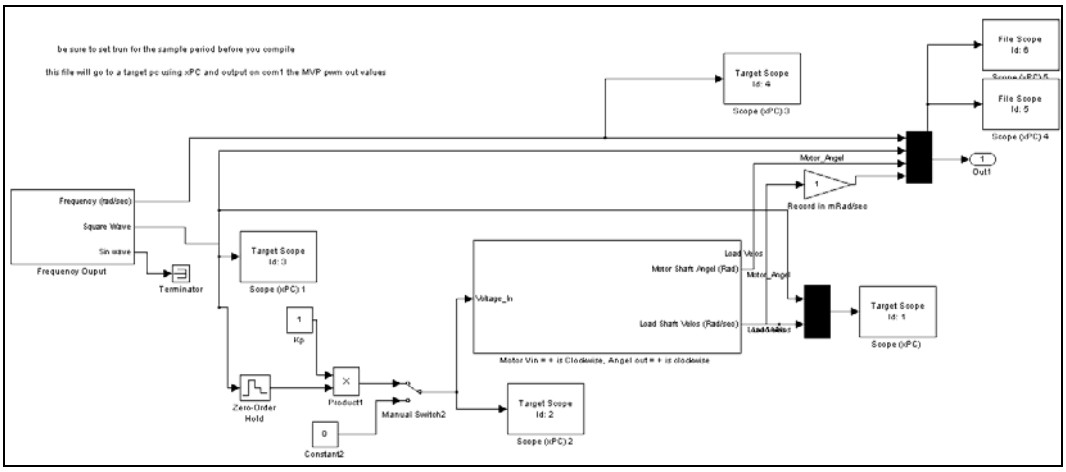

Figure 53: Simulink/xPC Frequency Response Main Diagram

The system is capable of running at a 20kHz sampling rate if there was no external communication. The RS232 connection is the major bottle neck in the speed of the system forcing the sampling period to 0.007sec or about 142Hz.

b. *System Verification*

Before testing could commence the system must be verified. To verify the test system a no load frequency response of the DC brushless motor [4] was taken and compared to that of the mathematical model of the DC motor in Figure 24. Figure 54 shows the frequency response plots of the DC motor [4] present in the

test rig in Figure 49. The motor in question has the parameters as listed in Table 1 and Table 2 and a frequency response plot as seen in Figure 24. Figure 54 shows the frequency response plot of the model of the DC motor, seen in Figure 24, plotted on top of the recoded frequency response data from the test rig.

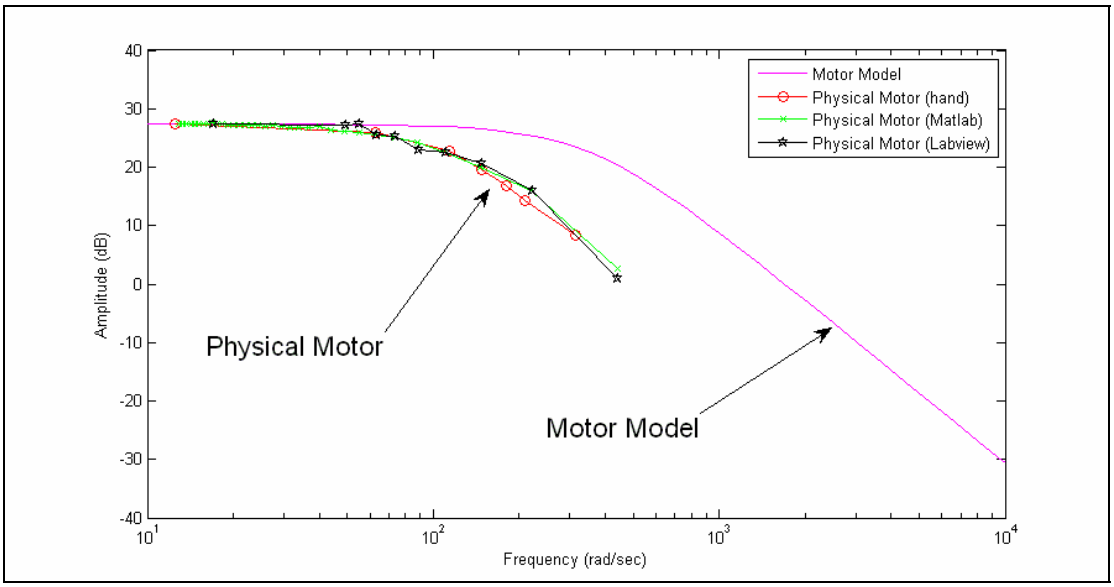

Figure 54: Frequency Response Plot of Brushless DC Motor [4] from: Model in Figure 23 with parameters from Table 1 and Table 2; Test Rig Measured by, Hand Using Matlab/xPC Recorded Data (hand), The Computer Using Matlab/xPC Recorded Data (Matlab), and Hand Using Labview Data (Labview)

An important observation about the frequency response data for the DC motor in Figure 54 is that the frequency response of the model does not match that of the frequency response of the physical system. This is an important observation because the model and frequency response of a DC motor are widely known. The motor used in the test rig included a data sheet which contained all of the parameters of the motor needed to make a proper model, Appendix C. To make sure that the error was not a reading or computational error the magnitudes from the test rig were calculated from two different sets of data. Each set of data was recoded over the same frequency range but were recorded with two different pieces of recording equipment. The two recording devices that were used was the RS232 encoder reader which sent the data directly back to the xPC system as well as the USB-DAQ-62ll data acquisition system which sent its recorded data back to the computer in to the Labview 8.0 software. In addition the magnitude of the

data gathered at a given frequency was calculated both via a computer program and by hand. All of the latter data was plotted on the same plot as data from the motor model simulation, see Figure 54.

When examining the data it was noted that the knee of the plot was not as sharp as it should have been if there were double poles on the real axis. In addition the slope of the recorded data is closer to negative 60dB/dec after the break point instead of the expected negative 40dB/dec. From this it was concluded that there was an extra pole in the system.

Figure 55 is the same frequency response plot as Figure 54 for the physical motor. The motor model however has been given an additional unity gain pole at -70rad/sec. The results from adding the third pole makes the simulated motor model match with the recorded data. The latter makes it apparent that the system has a third pole at around -70rad/sec somewhere in the system. This extra pole is a problem because it makes it difficult to see the TR in the system.

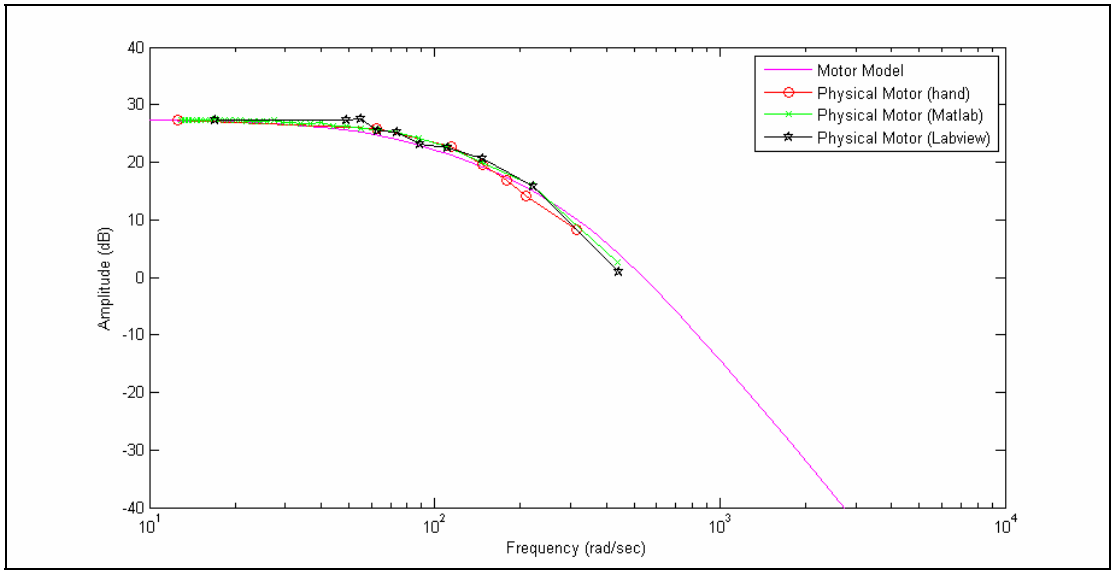

Figure 55: Frequency Response Data from the Physical Motor from Figure 54 and the Motor Model with an added pole at -70rad/sec

The fact that the data is the same when it was recorded using xPC (Matlab) and Labview means that the data recording software is not the source of the extra pole located at -70rad/sec. The two most like

candidates for the addition of the -70rad/sec pole in the system is the RS232 quadrature (4x) encoder reader [11] and the MVP2001 Single Axis Intelligent Drive [13] which is being used as a simple serial brushless DC motor driver. It is important to note that the counter clock speed for the NI-USB-6211, which is the data acquisition board that was used to read the encoders for verification, is 80MHz and the RS232 encoder reader [11] runs at 10MHz. Even though the counters on the NI-USB-6211 is much faster than those in the RS232 encoder reader each still recorded the same data. Therefore it is likely that the encoder reader is not the cause of the extra pole at -70rad/sec. The only item left in the system likely to have caused the extra pole at -70rad/sec is the MVP2001 [13].

Due to the extra pole in the system and the inability of removing it, short of getting a different DC motor driver, the system has not been verified and thus would not be able to give accurate results in experiments. A possible fix for this problem is to replace the MVP2001 with a dedicated brushless DC motor driver that has a bandwidth significantly higher than that of the motor.

Appendix G: Increasing the useable bandwidth of a system with TR via increasing the coupler's spring constant K_c

Using the transfer function of $\theta_a(s)/T(s)$ for the system exhibiting TR in Equation 10 the spring constant for the coupler, K_c, was increased to show the effects it has on the system. It is apparent from the frequency response of the latter system in Figure 56 that as the spring constant, K_c, is increased the w_r and w_{ar} frequencies are also increased. Due to the latter the maximum stable bandwidth of the system is also increased.

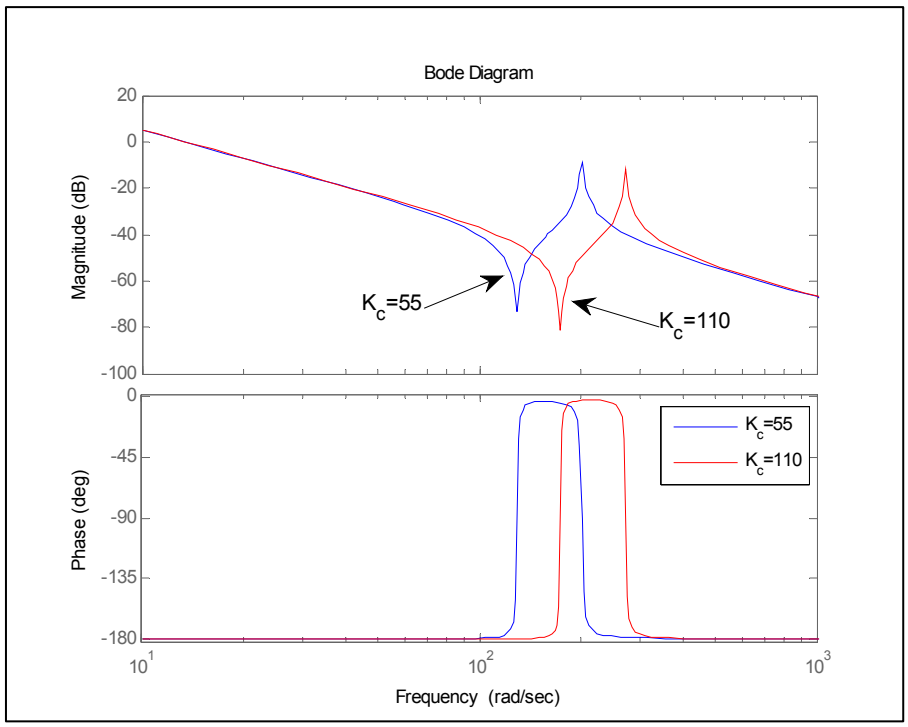

Figure 56: Frequency Response of Transfer Function $\theta_a(s)/T(s)$ from Equation 10 with the coupler's sprint constant K_c=55 oz/in (blue) and K_c=110 oz/in (red)

By doubling K_c the useable bandwidth of the system is not even increased by 100%. When increasing K_c the useable bandwidth is increased, however the cost in the physical parts with the higher spring constant are significantly higher. The latter method does not give a good return in bandwidth for the money invested.

Appendix H: Future Work

Future work on the subject of TR will include, but not limited to:

- Creation of partial state observers for a TR system.
- Implementation of RE using observers in simulation
- Implementation of SMC using observers in simulation
- Increase bandwidth of motor driver from TR test rig
- Increase bandwidth of Real Time control system for the TR test rig
- Implementation of RE using Real Time control on the TR test rig
- Implementation of SMC using Real Time control on the TR test rig